REPORT

All-perfluoropolymer, nonlinear stability-assisted monolithic surface combines topology-specific superwettability with ultradurability
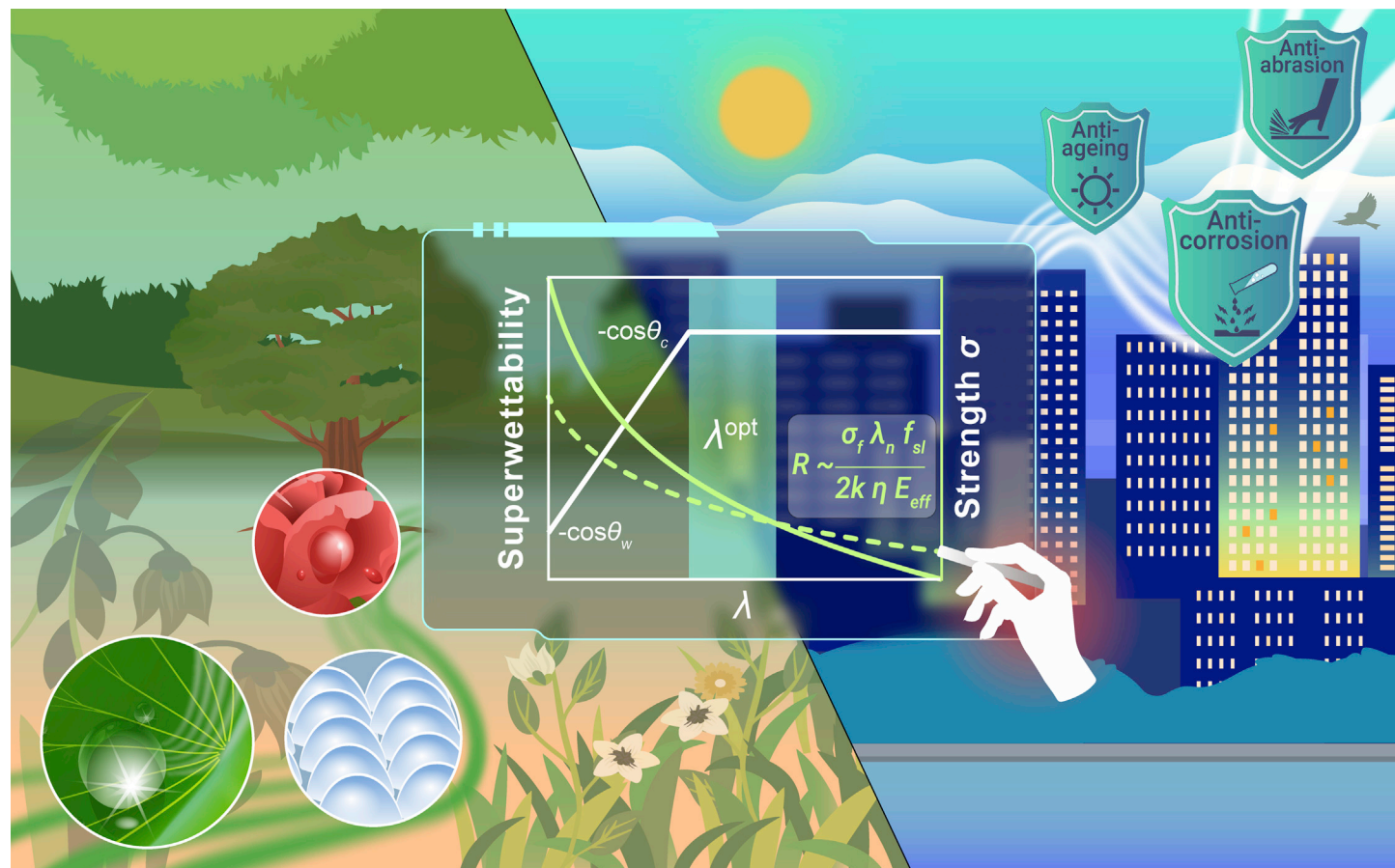
Wanbo Li,[1,6] Chiu-wing Chan,[1] Zeyu Li,[1] Sin-Yung Siu,[1] Siyu Chen,[1] Han Sun,[1] Zeyu Liu,[2] Yisu Wang,[1] Chong Hu,[1] Nicola Maria Pugno,[3,4] Richard N. Zare,[5] Hongkai Wu,[2,*] and Kangning Ren[1,7,8,*]

*Correspondence: chhkwu@ust.hk (H.W.); kangningren@hkbu.edu.hk (K.R.)

GRAPHICAL ABSTRACT

PUBLIC SUMMARY

- The monolithic perfluoropolymer surface (MPS) strategy enables biomimetic surfaces to combine geometric-material mechanics with topology-specific superwetting stability.

- The theoretical model predicted optimal structures and materials to realize simultaneously superwettability and ultradurability.

- The stability of the biomimetic surfaces was extended into a nonlinear range for further improving ultradurability.

- The MPS strategy helps to translate bioinspired surface principles into real-world applications.

All-perfluoropolymer, nonlinear stability-assisted monolithic surface combines topology-specific superwettability with ultradurability

Wanbo Li,[1,6] Chiu-wing Chan,[1] Zeyu Li,[1] Sin-Yung Siu,[1] Siyu Chen,[1] Han Sun,[1] Zeyu Liu,[2] Yisu Wang,[1] Chong Hu,[1] Nicola Maria Pugno,[3,4] Richard N. Zare,[5] Hongkai Wu,[2,*] and Kangning Ren[1,7,8,*]

[1]Department of Chemistry, Hong Kong Baptist University, Hong Kong 999077, China
[2]Department of Chemistry, The Hong Kong University of Science and Technology, Hong Kong 999077, China
[3]Department of Civil, Environmental and Mechanical Engineering, Laboratory of Bio-Inspired, Bionic, Nano, Meta Materials and Mechanics, Università di Trento, 38100 Trento, Italy
[4]School of Engineering and Materials Science, Queen Mary University of London, London E1 4NS, UK
[5]Department of Chemistry, Stanford University, Stanford, CA 94305, USA
[6]School of Mechanical Engineering, Shanghai Jiao Tong University, Shanghai 200240, China
[7]State Key Laboratory of Environmental and Biological Analysis, Hong Kong Baptist University, Hong Kong SAR 999077, China
[8]HKBU Institute of Research and Continuing Education, Shenzhen 518057, China
*Correspondence: chhkwu@ust.hk (H.W.); kangningren@hkbu.edu.hk (K.R.)

Developing versatile and robust surfaces that mimic the skins of living beings to regulate air/liquid/solid matter is critical for many bioinspired applications. Despite notable achievements, such as in the case of developing robust superhydrophobic surfaces, it remains elusive to realize simultaneously topology-specific superwettability and multipronged durability owing to their inherent tradeoff and the lack of a scalable fabrication method. Here, we present a largely unexplored strategy of preparing an all-perfluoropolymer (Teflon), nonlinear stability-assisted monolithic surface for efficient regulating matters. The key to achieving topology-specific superwettability and multilevel durability is the geometric-material mechanics design coupling superwettability stability and mechanical strength. The versatility of the surface is evidenced by its manufacturing feasibility, multiple-use modes (coating, membrane, and adhesive tape), long-term air trapping in 9-m-deep water, low-fouling droplet transportation, and self-cleaning of nanodirt. We also demonstrate its multilevel durability, including strong substrate adhesion, mechanical robustness, and chemical stability, all of which are needed for real-world applications.

INTRODUCTION

In nature, biological superhydrophobic skins often possess unique 3D microscale topologies that enable different specific interfacial functions for controlling surface matters.[1] A few examples include the nanopillar arrays on Cicada wings that promote transparency, self-cleaning, and mechanically rupturing cells;[2] the double reentrants on a springtail skin minimizing organic liquid wetting;[3] and the micro-papillae on a rose petal stabilizing water droplets at Wenzel wetting state.[4] For more examples, see Table S1. The exploration of these biological surfaces has inspired diverse topological functionalities, e.g., liquid detachment/adhesion,[5–9] gas entrapment,[10–12] anti-icing,[13–15] chemical shielding,[16] drag reduction,[17,18] oil/water separation,[19,20] heat transfer improvement,[21] and antibacteria activity.[22,23] While notable progress has been achieved in developing some biomimetic surfaces, such as in the case of superhydrophobic surfaces, there remains a major challenge to simultaneously control precise specific topology and realize the robustness of those biomimetic surfaces. In general, biomimetic surface functions require two essential components,[19,21,24–28] the specific 3D surface topologies and the surface chemistry of materials. However, both components are highly susceptible to material failure caused by stress concentration, short penetration distance for invasive matters, and the easy change of surface nature from hydrophobic to hydrophilic. Also, the need to construct the specific 3D architecture[29–34] recalls sophisticated manufacturing and limits material and structural options for enhancing robustness.

Recent years saw extensive efforts in translating bioinspired surfaces into real-world applications. For example, the surface robustness can be enhanced by introducing high-modulus materials[24,25,28,35,36] and perfluorinated chemistry[26,27,37] as manifested by those synthetic surface coatings. Yet, such coatings are commonly composed of disordered particles without microtopological controllability. Alternatively, "armor" structures (e.g., interconnected frames[29,38]

and pillars[30,39]) can be micromachined to protect weak nanostructures. But this strategy is specific to structural geometry and rigidity. To date, it remains an unresolved problem to develop versatile and scalable surfaces that simultaneously enable topology-specific functionality and ultradurability.[40]

Here, we present a nonlinear stability-assisted, monolithic perfluoropolymer surface (MPS) strategy to address the above challenge. In particular, MPS uses soft perfluoropolymers (sometimes referred to as Teflon, a commercial brand name) to make the entire coating, with all surface structures being part of this inert continuum. Using theoretical modeling and experimental validation, we found the MPS strategy combines geometric-material mechanics with superwetting stability well and suggests (1) an optimal structural design and preferential materials to simultaneously realize wetting and mechanical stability, and (2) the extension of the stability of the biomimetic surfaces into a nonlinear range. This principle is contrary to conventional wisdom—using highly rigid structures to bear the concentrated stress yet failing once slight inelastic deformation occurs. MPS was prepared in multiple-use models (coating, tape, and self-supporting film) through a modified high-temperature imprinting approach that is low-cost and scalable. We also demonstrated the versatility of MPS for efficiently regulating surface matter, as well as multilevel durability.

RESULTS

Surface design and fabrication

The MPS strategy is shown in Figures 1 and S1. We design all the surface structure parts of this monolithic continuum, which are firmly bonded to substrates without using any glue (Figure 1A). The geometric mechanics of soft material is explored to improve the durability of biomimetic surfaces (Figures 1B–1D). We first consider the mechanical stability of MPS with structural hierarchy n from three mechanical failure mechanisms: (1) friction-driven bending, (2) elastic instability, and (3) crushing of a hierarchical structure (see Text S1 for the details). Our modeling suggests that for a preferential material with low friction coefficient μ, moderate Young's modulus E, and high failure strength σ_f, the key to reaching mechanical robustness is to fulfill a geometric rule, that is, the structure slenderness λ'_n achieves the same resistance for mechanisms (1) and (2) when

$$\lambda'_n \sim \frac{\pi^2 E \mu}{2\sigma_f}$$

Moreover, when considering the wetting stability for MPS from the energy perspective,[41,42] a water droplet with a lower Gibbs free energy than the Wenzel wetting mode can be stabilized at the Cassie-Baxter state only for a slenderness larger than the critical value

$$\lambda''_n = \frac{1 - f_{sl}}{f_{sl}} \frac{1 + \cos \theta_Y}{\cos \theta_Y}$$

where θ_Y and f_{sl} are the Young's contact angle and the pillar area fraction of the surface, respectively. By coupling the evolution trends for maximizing
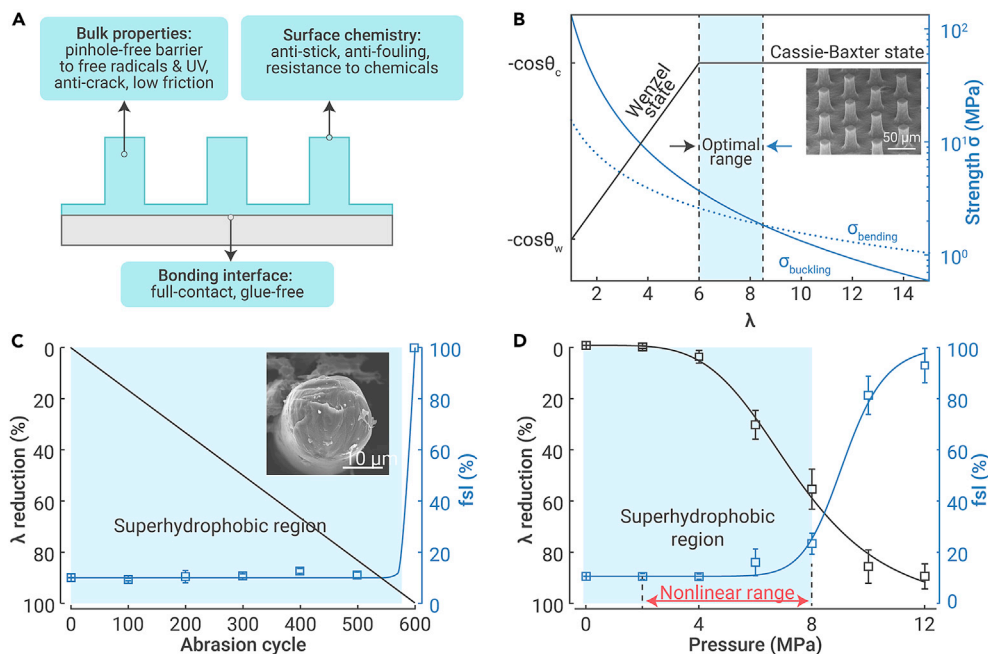
Figure 1. The MPS strategy coupling wetting and mechanical stability (A) A pillar model showing the MPS design for promoting outstanding chemical resistance, substrate adhesion, and eco-friendliness. (B) Change of theoretical wetting stability and influence of theoretical strength against buckling and bending of the pillar array as a function of the pillar slenderness λ. The light blue region indicates the optimal range for achieving both wetting and mechanical stability. (C and D) Experimental validation of the pillar strength based on a pillar array ($\lambda_0 = 8$) by plotting the change of the slenderness λ and liquid-solid contact fraction f_{ls} of the pillar array during repeated abrasion (C), and pressing under different apparent pressures (D), respectively. Data are mean ± SD from at least five independent measurements.

mechanical strength and stabilizing water repellency at the Cassie-Baxter state, the optimal slenderness λ_n^{opt} emerges between λ_n' and λ_n'', that is, this is achieved when $6 \leq \lambda_n^{opt} \leq 8.5$ (Figure 1B). As a result, when the wetting property is measured and the material is tough, it is found that the surface is highly abrasion-resistant (Figure 1C).

One essential part of our design is that the nonlinear dynamics of tough microstructures could be leveraged to strengthen mechanical robustness. As shown in Figure 1D, the tolerable compressive pressure of structures without losing wetting stability is much greater than the material failure strength using elastic deformation as the boundary condition, leading to an elevated resistance to crushing failure, with a robustness factor R being defined as

$$R \sim \frac{\sigma_{f \lambda_n f_{sl}}}{2k\eta E_{eff}}$$

where k is a constant on the order of the unity, η is the compaction index, and E_{eff} is the effective Young's modulus (see mechanism (iii) in Text S1 for the details). Such a geometry-based nonlinear mechanical behavior is also observed for many biological structures[43,44] and is counterintuitive to the common assumption that the biomimetic topological surfaces fail once inelastic deformation occurs. In the control experiments, this nonlinear regime collapses into the conventional one when the material toughness is reduced, that is, for structures made of materials with high hardness and large slenderness, fracture took place at the bottom and caused the immediate loss of preferential wettability (Figure S1).

Following the MPS design, we chose perfluoropolymer (MFA F1540, Solvay company) as the base material and developed a 3D high-temperature soft imprinting method to thermally fuse it (Text S2) with the substrate and create rational 3D microstructures on it (Figure 2A). The key to the method is a silicone thermal mold that possesses configurable elasticity and shape memory at extremely high temperatures (up to 350°C). Usually, such properties of normal silicones degrade rapidly owing to the scission of flexible molecular chains when heated.[36,45] To suppress degradation at elevated temperatures, we used iron nanoparticles to avoid the oligomer formation by binding the oxide's surface hydroxyl groups with silanol groups in the silicone mold, which also serves as soft crosslinks that maintain flexibility (Text S3 and Figure S2). In this way, we produced thousands of MPS products from one soft mold with improved fidelity within a short time (5 min per cycle). The products include transparent MPS coatings on different substrates (eg, glass, fabric, polyimide, and aluminum), self-supporting and flexible films, and tapes (Figures 2B–2D and S3). Such versatility makes MPS adaptive to different substrate and dynamic deformations. Collectively, the MPS strategy shows the promise of scalable and versatile biomimetic surfaces with topology-specific functionality and multipronged robustness.

Some topology-specific functions

In what follows, we demonstrate three examples of MPS for efficient regulating of air/liquid/solid matters (Figures 3 and S4). Although the surfaces commonly manifest two-tier structures in micro and nano scale, their wettability such as water contact angle θ^*, roll-off angle $\theta_{roll-off}$, droplet adhesion, pressure stability, and restitution coefficient can be very different (see Text S4 for details), and thus manifesting preferential yet strong superwettabilities. The first example is an air-trapping coating inspired by the springtail's skin (Figure 3A). As shown in Figures 3B and 3C, The MPS was imprinted with honeycomb cavity arrays with wetting resistance further strengthened by doubly reentrant edges. The sample could stably trap air in the cavities after being immersed under seawater with the extra pressure of ~90 kPa for 30 days, with a gas retention fraction $\varphi \sim$ 92.7% (where φ is the volume ratio between the entrapped gas and the cavity). The extra pressure was equivalent to that in ~9-m-deep water (Figure 3D), beyond the draft range of most ships. While the air-trapping surface could reduce the drag of marine vehicles, the inertness and anti-stickiness of perfluoropolymer endow the coating with enhanced corrosion and aging resistance, reduced microorganism adhesion, and outstanding robustness against cleaning operations. In addition, the reentrants can also be constructed on the top of an array of pillars, which made MPS effectively repellent to low-surface-energy liquids (Figure S5).

The second example is a rose petal-mimicking surface for a low-fouling droplet transfer (Figures 3E–3H). While prior works proposed the operation mechanism of adhesion-based droplet transfer, the functional application is still limited by the low sample compatibility and sample loss during transport caused by surface fouling, microdroplet residuals, and poor chemical tolerance. We conducted experiments to evaluate the MPS with regard to these challenges. As shown in Figures 3G, S6, and Video S1, a broad range of liquids (eg, serum, cell culture medium, and even 1-M NaOH) were compatible with our MPS, and minimal sample fouling was observed during transport, suggesting the functional robustness and generality of the surface. Meanwhile, all control samples made of normal lab materials, such as polystyrene (PS) and polypropylene (PP) even after surface fluorination protection, showed noticeable fouling/sample loss (Figure 3H). The observed difference between MPS and the control samples in droplet transfer performance could be attributed to two reasons. First, we design the structure edges of MPS to have convex micro-curvature, thus reduces the pinning effect to trigger capillary bridge rupturing,[46] whereas the previous report shows that structures with sharp edges inevitably pin microdroplets. Second, the MPS is a perfluoropolymer, which has a higher density of fluorine and mechanical stability than commonly used monolayer fluorinated coatings, one of the best anti-fouling coatings in past reports. As a result, MPS will enable a lower level of molecular fouling and reduce the chance of leaving residue droplets,[47] as demonstrated by control experiments shown in Figure 3H.

As a final example we mimic the lotus effect (Figures 3I–3M). An MPS containing hierarchical structures showed outstanding water repellence (Figure 3L). Even after being placed in the outdoor environment for 1 month, MPS can self-clean against nano-sized dirt (one major component of ambient fine particulate
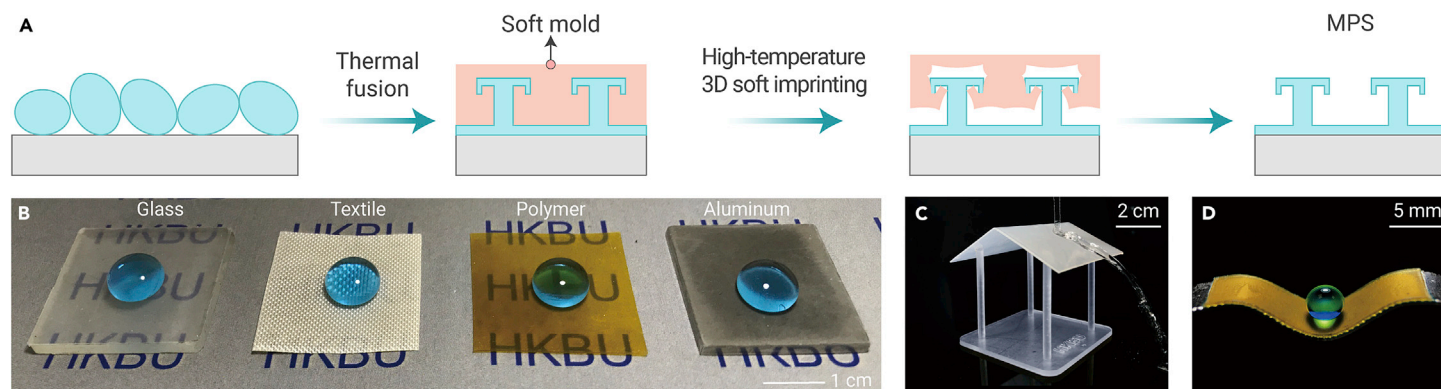
Figure 2. MPS Fabrication (A) Schematic illustration of fabrication method consisting of thermal fusion and high-temperature 3D soft imprinting. The method enables outstanding 3D topological controllability, substrate adhesion, and scale-up capability. (B–D) Photographs of MPS biomimetic materials, including coatings on diverse substrates (eg, glass, textile, PI, and aluminum) (B), a small shed made of a self-supporting superhydrophobic MPS membrane (C), and a composite tape stuck on a bent surface (D).

matters[48]) by impacting water droplets[49] (Figures 3M, S7, and S8). In contrast, the control surfaces possessing the same topology but made from other materials failed to self-clean under the same conditions (Figure 3M, Text S5, and Video S2, Part 2), demonstrating the rationale of our MPS design for improving self-cleaning performance.

Multilevel durability

We then evaluated the multilevel durability of MPS considering their mechanical strength (eg, substrate adhesion, structural toughness), chemical resistance to solvents and reactive substances, and weathering durability against radiant heat and moisture. Considering the delicate structure and possibly least robustness among all the samples, we used the lotus-mimicking sample in these tests. First, a standard shear-stress model recorded ~5.66 MPa substrate adhesion of our MPS, which was even stronger than 3M PR1500 (Figure 4A), a strong and multi-purpose glue. The bonding was so strong that during detaching, the cracks took place in the MFA layer rather than at the bonding interface, as evidenced by the elementary composition (Figure 4B), microscopic morphology, and wettability of the substrate surface (Figure S9). To cross-compare, we also performed the tape-peeling test frequently used in past reports.[26,29] Here we used a rubbery adhesive peeling test to upgrade the test. Though some commercial coatings could sustain certain cycles of tape peeling, rubbery adhesive peeling immediately reveal their insufficient bonding strength (Figure S10A). In sharp contrast, MPS did not present noticeable deterioration after thousands of rounds of tape peeling and hundreds of rubbery adhesive peeling. Moreover, our MPS is highly flexible—an MFA-glass fiber hybrid film passed more than 100,000-cycle folding (Figures S10B and S10C).

We evaluated the structural strength of the coating using two models: crushing and abrasion (Figure S11). During the crushing test, our MPS did not show any noticeable change after exposure to 300 kPa loads, as plotted in Figure 4C. When the load reached 500 kPa, the surface showed deteriorated hydrophobicity ($\theta^* \sim 154.6°$ and $\theta_{roll-off} \sim 10.8°$). These pressures were far beyond the ground pressure of a human adult (~50 kPa), a military tank (~100 kPa), and an elephant (~250 kPa) (Figure 4C). In the abrasion test, the surface of the MPS maintained water repellence over ~1500-cycle abrasions (Figure 4D). As could be explained by our friction-bending model, the microstructures on the MPS surface will not be torn down. Instead, dense nano-sized hairs are continuously regenerated on the tops of the micropillars (Figure S12), realizing a self-regeneration effect until the surface texture was worn away after ~1,800-cycle abrasions. MPS also passed challenging tests mimicking real-world wearing conditions (Videos S3 and S4), illustrating our MPS materials' remarkable robustness. In control experiments, all the samples, commercial products, and surfaces similar to the existing reports[50] lose superhydrophobicity simply after a few finger wipes (Video S5).

Chemical resistance to corrosive vapors and aging was also tested. Distinguished from the conventional liquid immersion model, we treated the samples with saturated corrosive vapors. We consider it a more meaningful test for the chemical robustness of a superhydrophobic coating, as the vapor can easily penetrate the air cushion to destroy the coating or even the underlying substrate. We found MPS can survive various corrosive gas/vapor (eg, strong acid, alkali, oxidant, and organic solvent) for more than 7 days (Figure 4E). Moreover, in an

accelerated aging test, MPS did not show any noticeable decay in water repellency throughout this entire test, indicating its prolonged lifespan in real-world weathering. In sharp contrast, control samples turned hydrophilic within 1 day (Figures 4F and S13 and Video S6). We also tested our coatings under even harsher conditions, which can appear in many situations in industrial, high-altitude, and even space environments. These test conditions include sonication in strong chemicals listed in Figure 4E, exposure to 185-nm UV radiation for 7 days, and heating at 200°C for 7 days (Figure S14). The MPS remained intact after all these tests.

DISCUSSION

The advantages of MPS over superhydrophobic surfaces produced by conventional strategies (see Table S2 for the details) are summarized using some qualitative evaluation indices in a radar map (Figure 5). The details of the rubrics are presented in Table S3. The MPS achieved performances comparable to best records in multiple aspects, eg, peeling, abrasion, crushing, and chemical/aging resistance. Also, MPS favors eco-friendliness by minimizing the release of microplastics and nanomaterials, which is impossible for those nanoparticle-based coatings. Moreover, the fabrication cost of the MPS strategy (estimated at within 10 \$/m²) is competitive, especially considering its capability to create large-scale arrays of precisely defined true-3D microstructures and outstanding durability. Altogether, the MPS strategy has demonstrated the capability to simultaneously realize topology-specific functionality and multilevel robustness for the control of gas/liquid/solid matters, which may fulfill the challenging requirements for real-world applications in air trapping, liquid transport, and self-cleaning, as well as many other possible applications, such as anti-icing, anti-corrosion, heat transfer, and drag reduction.

MATERIAL AND METHODS
Test the stabilities of the soft pillars

For validating theoretical prediction, the mechanical strength of pillars ($\lambda \sim 8$, $f_{sl} \sim 10\%$) against abrasion, pressing, and buckling was tested. For the abrasion test, the pillar array (2 × 2 cm²) was brought into contact with a 1,200-Cw sandpaper, and a weight of 100 g was applied. The sample was pushed forward 10 cm along the ruler and then backward to the original point. Then the sample was rotated by 90°, and the movement was repeated. This procedure is defined as one abrasion cycle. The cycle was repeated to test the sample's abrasion robustness. For the press test, fixed loads (from 0 to 16 MPa) were applied on the samples (1 × 1 cm²) for 10 min. After the abrasion and pressing tests, the pillar geometries (ie, pillar length l, pillar diameter D, and center-to-center distance d) were characterized with scanning electron microscopy (SEM). The Cassie-Baxter theory suggests that, for the pillar array with an inherent water contact angle $\theta_Y \sim 110°$, f_{sl} must be lower than 20% to allow $\theta^* \geq 150°$. Thus, pillars that have $f_{sl} > 20\%$ were considered lost superhydrophobicity. For comparison, polypropylene (PP) and polystyrene (PS) samples with the same surface architecture were also tested.

Fabrication of MPS

The MPS was fabricated by thermally bonding perfluoropolymer on substrates (eg, glass, textile, polyimide [PI], and aluminum plate) and imprinting 3D structures onto the surface. For bonding perfluoropolymer with a substrate, perfluorinated polymers (eg, MFA F1540, Solvay
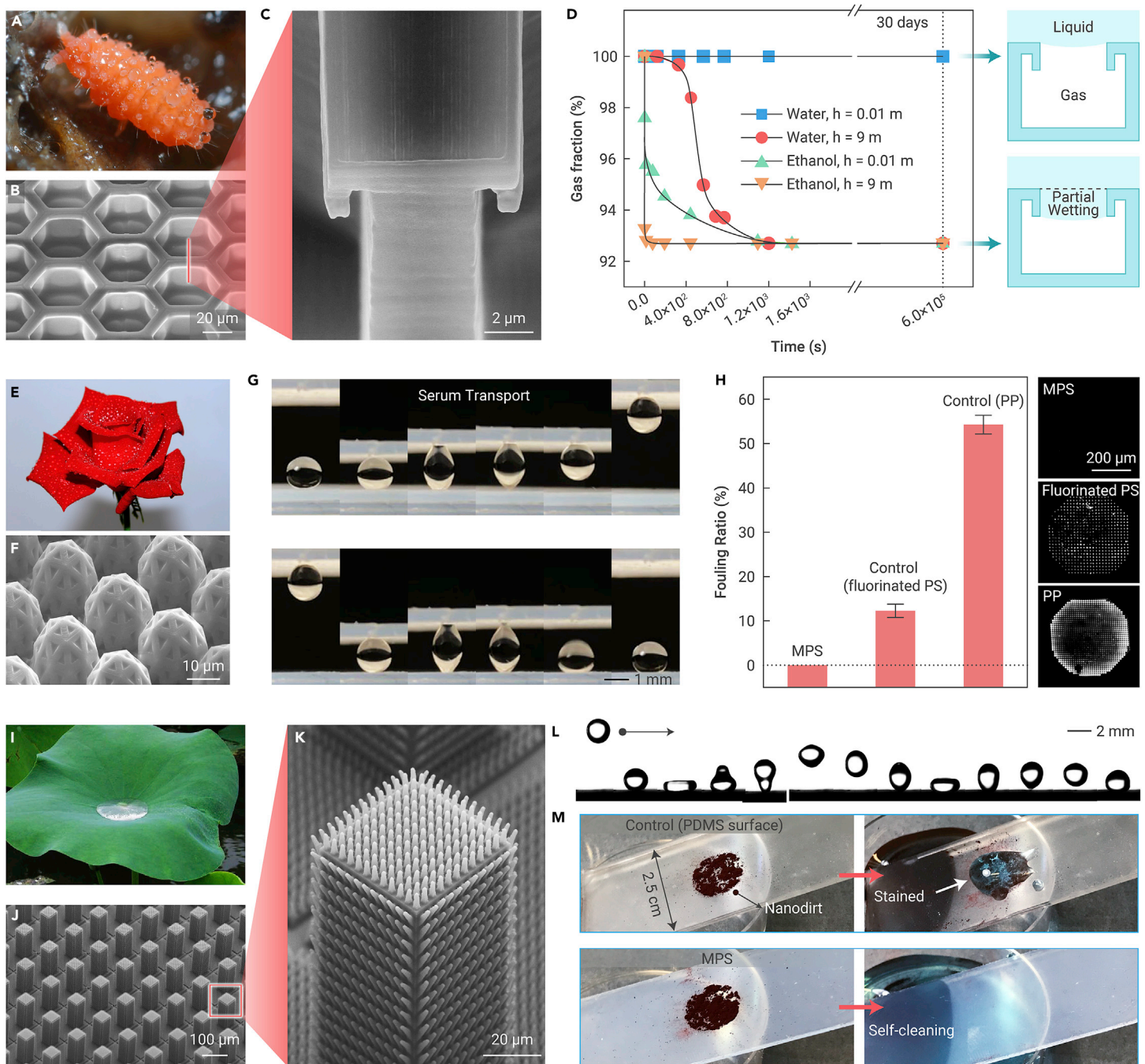
Figure 3. Topology-specific functionalities (A−D) MPS comprising cavities with doubly reentrants mimicking the skin structure of a springtail beetle for effective air trapping. (A) Optical image of a springtail. Image courtesy of Jan J. van Duinen (photographer). (B and C) SEM image of the cavity array (B) and the doubly reentrants (C). (D) The relationship between the fraction of entrapped air in the cavities and the immersion time. The scheme illustrates two models of liquid suspending at the first and second reentrant, respectively. (E−H) MPS comprising micro protuberances mimicking the rose petal for low-fouling liquid droplet transportation. (E) Optical image of a rose flower with a high adhesion to water droplets. (F) SEM images of the MPS micro protuberances. (G) Optical images showing a droplet of serum transported between two MPS surfaces. (H) Measurement of the sample loss during transport. The MPS surface is free of observable fouling, while the counterparts, surfaces made of PP and fluorinated PS, suffer from serious fouling by bioanalytes. (I−M) Hierarchical MPS pillar array mimicking the lotus effect. (I) Image of a superhydrophobic lotus leaf. (J and K) SEM images showing the hierarchical topology of the pillar array (J) and the hierarchical unit (K). (L) Optical image showing the bouncing of a water droplet on the lotus-mimicking surface. (M) Representative images show the dirt removal tests. Only MPS surface showed self-cleaning property against nano-sized dirt (~200-nm in diameter), as compared with control surfaces (Video S2). Data are mean ± SD from at least five independent measurements.

company) were laminated with the substrates at 350°C for 10 min, and then cooled to 200°C, with the pressure maintained at 0.5 MPa (see Text S2 for details). After that, the perfluoropolymer layer on the substrate was textured using 3D imprinting as described below.

Before the 3D imprinting process, master structures with predesigned texture were fabricated by 3D printing. To prepare for the 3D imprinting, a thermally stable mold was cast from the master (for details, see Figure S2); then, the perfluoropolymer layer on the substrate was imprinted by the thermal mold at 280°C for 1 min under 0.1 MPa. MPS was finally collected after cooling to room temperature. Both the master and the soft mold could be reused for scalable manufacturing.

MPS in different use modes, ie, coatings, membranes, and adhesive tapes, were fabricated as illustrated in Figure S3. For producing the self-supporting MPS membrane, a perfluoropolymer film is directly imprinted. For producing the adhesive tape, MPS was first fabricated on a polyimide (PI) film and then an adhesive is coated on the other side of the PI film.

Characterization of the hydrophobicity

The hydrophobicity of the materials was characterized by measuring the static water contact angle (θ^*) and the roll-off angle ($\theta_{roll-off}$). To characterize θ^*, the optical image of a 5-μL water droplet on a horizontal surface was taken, and then the angle within the liquid body
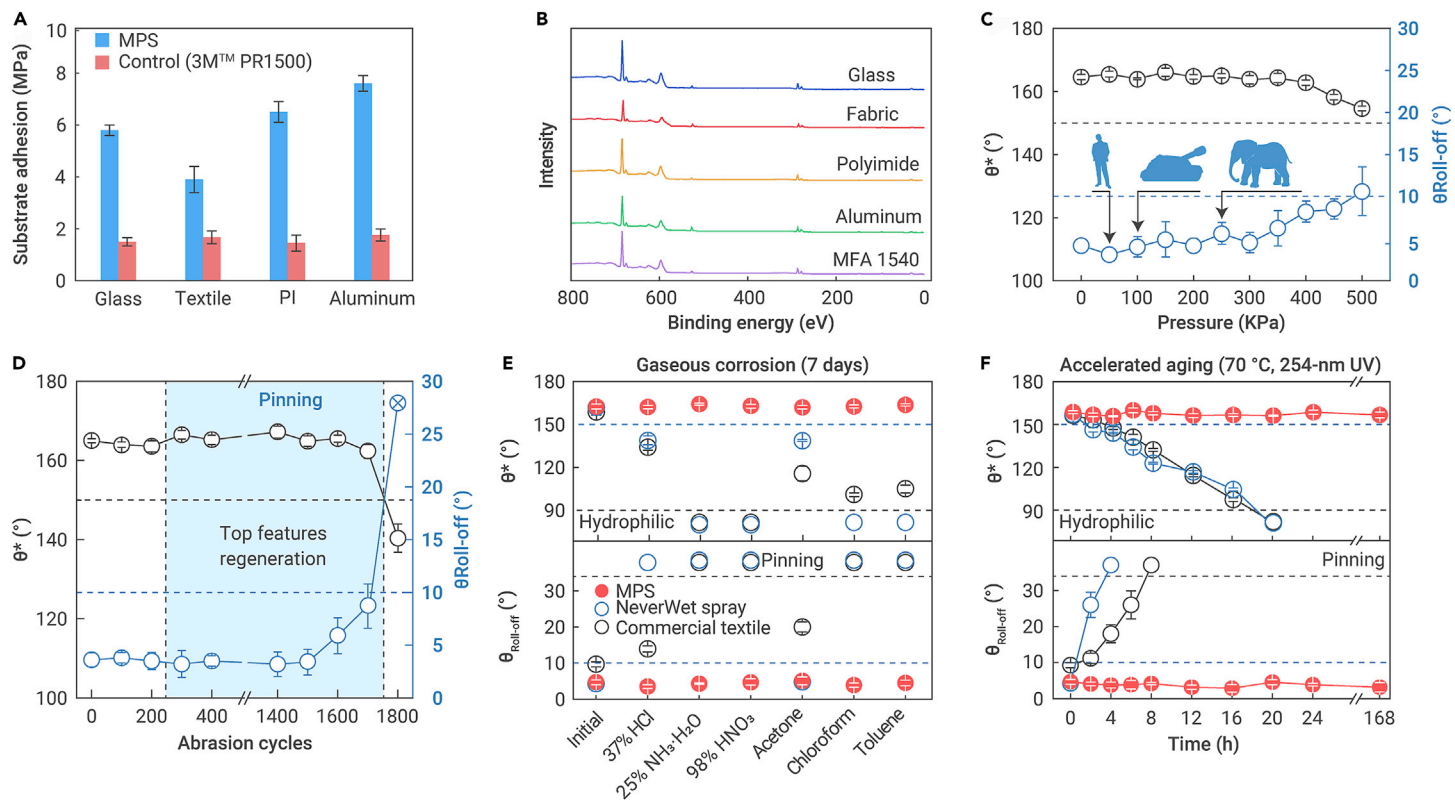
Figure 4. Multipronged robustness (A and B) Substrate adhesion. (A) Adhesion strength of MPS with various substrates compared with the commercial glue 3M PR1500. (B) XPS spectrum of the substrate surfaces after the perfluoropolymer layers were detached in the tests. The spectra are identical to that of MFA F1540. (C and D) Mechanical robustness. (C) Relationship between water repellence and apparent pressure applied to the surface in Figure 2E. For comparison, the ground pressure of an adult man, a military tank, and an elephant, respectively, are denoted in the insets. (D) Relationship between the water repellence of the surface in Figure 2E and abrasion cycles. (E and F) Chemical and aging robustness. (E) Water repellence of the MPS before and after treatment with strong gaseous chemicals (acid, alkali, oxidant, and organic solvents) for 1 week. (F) Evolution of the water repellence of three superhydrophobic materials during accelerated aging. In (C)−(F), the black and blue dash lines denote the boundaries of superhydrophobicity ($\theta^* > 150°$ and $\theta_{roll\text{-}off}$ <10°). In (E) and (F), a commercial NeverWet spray and water-repellence textile were also tested to provide reference index of the chemical and weathering stability. Data are mean ± SD from at least five independent measurements.

between the liquid-gas and liquid-solid lines was measured. To characterize $\theta_{roll\text{-}off}$, a 10-μL droplet was placed on the horizontal surface and the sample surface was tilted gradually at a resolution of 0.1°. The critical angle that enables the droplet to start rolling was recorded as $\theta_{roll\text{-}off}$. In each case, five replicates of each measurement were performed to calculate the standard deviation.

Air trapping

To test the trapping performance, the samples were immersed in seawater and the air bubbles trapped inside the sample surface were photographed with an optical microscope. To evaluate the trapping efficiency, the sample immersed in water was placed in a sealed container, which was then pressurized to different pressures (0, 20, 40, 60, 80, and

90 kPa compared with normal pressure) for 24 h. Optical images were taken afterward and analyzed using ImageJ software (National Institutes of Health). The trapping efficiency was defined as the volume ratio between the air retentate and the cavities.

Droplet transportation

To test the transportation, a liquid droplet was first placed on a low-adhesion superhydrophobic surface, and was then captured by a high-adhesion surface upside down; finally, the droplet was transported to another high-adhesion MPS surface. To demonstrate the anti-corrosion capability, a droplet of 1-M NaOH was used. To demonstrate the anti-fouling performance, a droplet of fluorescently labeled globulin solution was adhered on the high-adhesion surface upside down for 30 min, and then transported to another high-adhesion
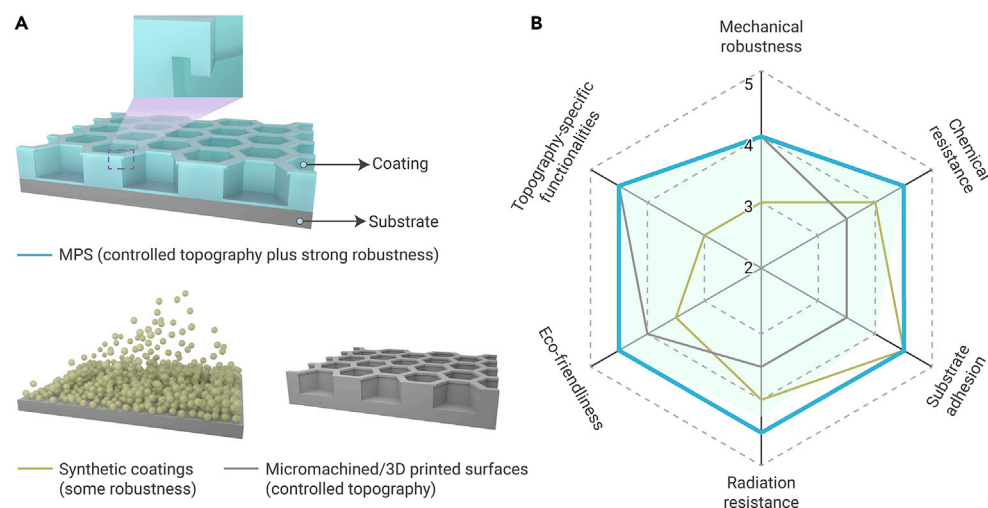
Figure 5. MPS combines topological controllability and multilevel durability (A) Illustration of two major groups of existing strategies (lower schematics), i.e., synthetic coatings and micromachined/3D printed surface, as well as MPS strategy (upper schematic) for preparing biomimetic surfaces. (B) A radar map showing the qualitative indexes of the characters of biomimetic coatings produced using different strategies (see references and rubrics in Tables S2 and S3). The potential applications, e.g., anti-icing and drag reduction, require multipronged merits of biomimetic coatings (light green area). MPS biomimetic surfaces (light blue line) can fulfill the multipronged requirements, addressing the limitations of synthetic coatings (gray line) and micromachined/3D printed coatings (dark yellow line).

surface, after which, a fluorescence image was taken to identify the fouled area. The fouling ratio was defined as the projected area ratio between the fouled area and the surface.

Self-cleaning test

The self-cleaning tests were performed by using iron oxide particles to mimic dirt contamination on the MPS surfaces. Superhydrophobic surfaces made of different materials, ie, PDMS, polyethylene (PE), and PP, with the same topology were used for comparison. The iron oxide (Fe_3O_4) particles were first spread on the tested surfaces and tapped gently to ensure that they have close contact with the surfaces. Water was then dropped onto the surfaces to remove the particles. To investigate the effect of particle size on the self-cleaning property of the tested surfaces, $\sim$2-μm and $\sim$200-nm iron oxide particles were used as the mimetic dirt. Pining of water droplets on a tested surface was used as the evidence of a surface failing to self-clean.

Substrate adhesion tests

The substrate adhesion of MPS was characterized by the shear-stress model. The tested substrate was sandwiched between two aluminum plates, and the interfaces were thermally bonded by a perfluoropolymer thin film. The bonded area was 25 × 20 mm^2. To realize the bonding, the sandwiched samples were laminated at 350°C for 10 min and then cooled to room temperature. The bonding strength was measured with a tensiometer, where the stress was recorded as a function of the longitudinal extension regulated at a speed of 5 mm/min. After detaching, the contact angle measurement, SEM imaging, and X-ray photoelectron spectroscopy (XPS) were conducted to investigate the fracture interfaces.

The adhesion strength was further tested by using tape peeling and repeated folding. The peeling test used a pressure-sensitive rubbery adhesive (Blu Tack, Bostik), which can fill the texture of rough surfaces rather than only adhere to the very top of surface structures. After laminating with the tested surfaces under $\sim$500 kPa for 5 min, the rubbery adhesive was peeled off slowly.

Folding test

A folding test was conducted to evaluate the material flexibility by the reciprocated folding model. The water repellence ($\theta*$ and $\theta_{roll-off}$) was recorded after every 10,000 cycles to characterize the robustness of the sample.

Chemical and aging tests

The chemical robustness of the MPS was tested against gaseous corrosives, aging conditions, and other harsh environments. A commercial superhydrophobic spray (NeverWet) and a water-repelling textile were comparatively tested. To evaluate the robustness against gaseous corrosives, samples and corrosive chemicals were placed inside a sealed container, which was then evacuated to 90 kPa to generate a saturated corrosive gas atmosphere. The chemicals included 37% HCl, 25% $NH_3 \cdot H_2O$, 98% HNO_3, acetone, chloroform, and toluene, respectively. The duration for each test was 7 days. For the accelerated aging test, samples were exposed to 254-nm UV radiation at 70°C and 70% relative humidity. For the harsh environments test, fresh samples were exposed to ultrasonication (40 kHz) in the above chemicals for 1 h, 185-nm UV radiation for 7 days, air plasma for 30 min, and 200°C heat for 7 days. The water repellence ($\theta*$ and $\theta_{roll-off}$) of these samples was measured during and after these tests for determining durability.

Thermal stability

To investigate the thermal stability of the MPS, we heated a superhydrophobic MPS, a high-quality commercial water-repelling spray (NeverWet), and a commercial water-repelling textile at 200°C for 1 day. We found that the color of the commercial products faded seriously, and their surfaces became hydrophilic, whereas the MPS remained superhydrophobic. After being heated at 250°C for 1 week, the MPS superhydrophobic surface was still intact.

REFERENCES

1. Liu, M., Wang, S., and Jiang, L. (2017). Nature-inspired superwettability systems. Nat. Rev. Mater. **2**, 17036.
2. Ivanova, E.P., Hasan, J., Webb, H.K., et al. (2012). Natural bactericidal surfaces: mechanical rupture of pseudomonas aeruginosa cells by cicada wings. Small **8**, 2489–2494.
3. Helbig, R., Nickerl, J., Neinhuis, C., and Werner, C. (2011). Smart skin patterns protect springtails. PLoS One **6**, e25105.
4. Feng, L., Zhang, Y., Xi, J., et al. (2008). Petal effect: a superhydrophobic state with high adhesive force. Langmuir **24**, 4114–4119.
5. Bird, J.C., Dhiman, R., Kwon, H.-M., and Varanasi, K.K. (2013). Reducing the contact time of a bouncing drop. Nature **503**, 385–388.
6. Liu, Y., Moevius, L., Xu, X., et al. (2014). Pancake bouncing on superhydrophobic surfaces. Nat. Phys. **10**, 515–519.
7. Tan, Y., Hu, B., Chu, Z., and Wu, W. (2019). Bioinspired superhydrophobic papillae with tunable adhesive force and ultralarge liquid capacity for microdroplet manipulation. Adv. Funct. Mater. **29**, 1900266.
8. Feng, S., Zhu, P., Zheng, H., et al. (2021). Three-dimensional capillary ratchet-induced liquid directional steering. Science **373**, 1344–1348.
9. Hu, S., Cao, X., Reddyhoff, T., et al. (2022). Pneumatic programmable superrepellent surfaces. Droplet **1**, 48–55.
10. Zhu, P., Kong, T., Tang, X., and Wang, L. (2017). Well-defined porous membranes for robust omniphobic surfaces via microfluidic emulsion templating. Nat. Commun. **8**, 15823.
11. Hensel, R., Finn, A., Helbig, R., et al. (2014). Biologically inspired omniphobic surfaces by reverse imprint lithography. Adv. Mater. **26**, 2029–2033.
12. Li, X., Zhang, J., Wang, X., et al. (2022). Bio-inspired spontaneous splitting of underwater bubbles along a superhydrophobic open pathway without perturbation. Droplet **1**, 65–75.
13. Wu, S., Du, Y., Alsaid, Y., et al. (2020). Superhydrophobic photothermal icephobic surfaces based on candle soot. Proc. Natl. Acad. Sci. USA **117**, 11240–11246.
14. Yao, Y., Zhao, T.Y., Machado, C., et al. (2020). Frost-free zone on macrotextured surfaces. Proc. Natl. Acad. Sci. **117**, 6323–6329.
15. Gurumukhi, Y., Chavan, S., Sett, S., et al. (2020). Dynamic defrosting on superhydrophobic and biphilic surfaces. Matter **3**, 1178–1195.
16. Pan, S., Kota, A.K., Mabry, J.M., and Tuteja, A. (2013). Superomniphobic surfaces for effective chemical shielding. J. Am. Chem. Soc. **135**, 578–581.
17. Lee, C., and Kim, C.J. (2011). Underwater restoration and retention of gases on superhydrophobic surfaces for drag reduction. Phys. Rev. Lett. **106**, 014502.
18. Xu, M., Sun, G., and Kim, C.J. (2014). Infinite lifetime of underwater superhydrophobic states. Phys. Rev. Lett. **113**, 136103.
19. Zhang, W., Shi, Z., Zhang, F., et al. (2013). Superhydrophobic and superoleophilic PVDF membranes for effective separation of water-in-oil emulsions with high flux. Adv. Mater. **25**, 2071–2076.
20. Gao, X., Zhou, J., Du, R., et al. (2016). Robust superhydrophobic foam: a graphdiyne-based hierarchical architecture for oil/water separation. Adv. Mater. **28**, 168–173.
21. Li, G., Hong, G., Dong, D., et al. (2018). Multiresponsive graphene-aerogel-directed phase-change smart Fibers. Adv. Mater. **30**, 1801754.
22. Tesler, A.B., Kim, P., Kolle, S., et al. (2015). Extremely durable biofouling-resistant metallic surfaces based on electrodeposited nanoporous tungstite films on steel. Nat. Commun. **6**, 8649.
23. Privett, B.J., Youn, J., Hong, S.A., et al. (2011). Antibacterial fluorinated silica colloid superhydrophobic surfaces. Langmuir **27**, 9597–9601.
24. Deng, X., Mammen, L., Butt, H.J., and Vollmer, D. (2012). Candle soot as a template for a transparent robust superamphiphobic coating. Science **335**, 67–70.
25. Lu, Y., Sathasivam, S., Song, J., et al. (2015). Robust self-cleaning surfaces that function when exposed to either air or oil. Science **347**, 1132–1135.
26. Peng, C., Chen, Z., and Tiwari, M.K. (2018). All-organic superhydrophobic coatings with mechanochemical robustness and liquid impalement resistance. Nat. Mater. **17**, 355–360.
27. Pan, S., Guo, R., Björnmalm, M., et al. (2018). Coatings super-repellent to ultralow surface tension liquids. Nat. Mater. **17**, 1040–1047.
28. Li, Z., Cao, M., Li, P., et al. (2019). Surface-embedding of functional micro-/nanoparticles for achieving versatile superhydrophobic interfaces. Matter **1**, 661–673.
29. Wang, D., Sun, Q., Hokkanen, M.J., et al. (2020). Design of robust superhydrophobic surfaces. Nature **582**, 55–59.
30. Kondrashov, V., and Rühe, J. (2014). Microcones and nanograss: toward mechanically robust superhydrophobic surfaces. Langmuir **30**, 4342–4350.
31. Liu, T.L., and Kim, C.J. (2014). Turning a surface superrepellent even to completely wetting liquids. Science **346**, 1096–1100.
32. Yun, G.T., Jung, W.B., Oh, M.S., et al. (2018). Springtail-inspired superomniphobic surface with extreme pressure resistance. Sci. Adv. **4**, eaat4978.
33. Gonzalez-Avila, S.R., Nguyen, D.M., Arunachalam, S., et al. (2020). Mitigating cavitation erosion using biomimetic gas-entrapping microtextured surfaces (GEMS). Sci. Adv. **6**, eaax6192.
34. Domingues, E.M., Arunachalam, S., Nauruzbayeva, J., and Mishra, H. (2018). Biomimetic coating-free surfaces for long-term entrapment of air under wetting liquids. Nat. Commun. **9**, 3606.
35. Mates, J.E., Bayer, I.S., Palumbo, J.M., et al. (2015). Extremely stretchable and conductive water-repellent coatings for low-cost ultra-flexible electronics. Nat. Commun. **6**, 8874.
36. Li, W., Yu, M., Sun, J., et al. (2019). Crack engineering for the construction of arbitrary hierarchical architectures. Proc. Natl. Acad. Sci. USA **116**, 23909–23914.
37. Zhang, L., Zhou, A.G., Sun, B.R., et al. (2021). Functional and versatile superhydrophobic coatings via stoichiometric silanization. Nat. Commun. **12**, 982.
38. Verho, T., Bower, C., Andrew, P., et al. (2011). Mechanically durable superhydrophobic surfaces. Adv. Mater. **23**, 673–678.
39. Schutzius, T.M., Jung, S., Maitra, T., et al. (2015). Spontaneous droplet trampolining on rigid superhydrophobic surfaces. Nature **527**, 82–85.
40. Dhyani, A., Wang, J., Halvey, A.K., et al. (2021). Design and applications of surfaces that control the accretion of matter. Science **373**, 294.
41. Zheng, Q.S., Yu, Y., and Zhao, Z.H. (2005). Effects of hydraulic pressure on the stability and transition of wetting modes of superhydrophobic surfaces. Langmuir **21**, 12207–12212.
42. Panter, J.R., Gizaw, Y., and Kusumaatmaja, H. (2019). Multifaceted design optimization for superomniphobic surfaces. Sci. Adv. **5**, eaav7328.
43. Carpinteri, A., and Pugnø, N. (2005). Are scaling laws on strength of solids related to mechanics or to geometry? Nat. Mater. **4**, 421–423.

44. Cranford, S.W., Tarakanova, A., Pugno, N.M., and Buehler, M.J. (2012). Nonlinear material behaviour of spider silk yields robust webs. Nature **482**, 72−76.

45. Ren, K., Dai, W., Zhou, J., et al. (2011). Whole-Teflon microfluidic chips. Proc. Natl. Acad. Sci. USA **108**, 8162−8166.

46. Krumpfer, J.W., Bian, P., Zheng, P., et al. (2011). Contact angle hysteresis on superhydrophobic surfaces: an ionic liquid probe fluid offers mechanistic insight. Langmuir **27**, 2166−2169.

47. Carré, A., Gastel, J.C., and Shanahan, M.E.R. (1996). Viscoelastic effects in the spreading of liquids. Nature **379**, 432−434.

48. Kleeman, M.J., and Cass, G.R. (1998). Source contributions to the size and composition of urban particulate air pollution. Atmos. Environ. **32**, 2803−2816.

49. Shi, S., Lv, C., and Zheng, Q. (2019). Drop impact on two-tier monostable superrepellent surfaces. ACS Appl. Mater. Interfaces **11**, 43698−43707.

50. Nilsson, M.a., Daniello, R.J., and Rothstein, J.P. (2010). A novel and inexpensive technique for creating superhydrophobic surfaces using Teflon and sandpaper. J. Phys. D Appl. Phys. **43**, 045301.

AUTHOR CONTRIBUTIONS

K.N.R. and H.K.W. conceived the idea and led the project. W.B.L., K.N.R., and H.K.W. designed the experiments. W.B.L., C.W.C., Z.Y.L., S.Y.S., S.Y.C., H.S., Z.Y.L., Y.S.W., and C.H. conducted the experiments and analyzed the data. N.M.P. built the theoretical model. W.B.L., N.M.P., R.N.Z., H.K.W., and K.N.R. wrote the paper. All authors discussed the results and commented on the manuscript.

DECLARATION OF INTERESTS

The authors declare no competing interests.

SUPPLEMENTAL INFORMATION

It can be found online at https://doi.org/10.1016/j.xinn.2023.100389.

LEAD CONTACT WEBSITE

https://renkangning.wixsite.com/rengroup.

Supplemental Information

All-perfluoropolymer, nonlinear stability-assisted monolithic surface combines topology-specific superwettability with ultradurability

Wanbo Li, Chiu-wing Chan, Zeyu Li, Sin-Yung Siu, Siyu Chen, Han Sun, Zeyu Liu, Yisu Wang, Chong Hu, Nicola Maria Pugno, Richard N. Zare, Hongkai Wu, and Kangning Ren

1 **Supporting Information Text**

2 **1. Modelling and material design of monolithic perfluoropolymer surface (MPS)**

3 In this section we rationalize the pillar strength thanks to simple and fundamental laws also

4 useful for the preliminary robust design of these hierarchical soft surfaces. The mechanical

5 robustness has been demonstrated mainly against three different compression mechanisms:

6 friction (i), instability (ii), and crushing (iii).

7 (i) When compression by a force N is applied at the top of a pillar and sliding is further

8 imposed, a shear/friction force is generated at its top; accordingly, bending stress emerges

9 at the pillar clamp, namely $\sigma_0 = \frac{2\mu N}{\pi r_0^2} \lambda_0 = 2\mu p \lambda_0$, where μ is the friction coefficient

10 between the compressive element and the Teflon, r_0 is the pillar radius, $\lambda_0 = 2l_0/r_0$ is the

11 pillar slenderness, and p is the applied nominal pressure. If a first hierarchical level of n

12 pillars is added, their radius is $r_1 = r_0\sqrt{\frac{f_{sl}}{n}}$ where f_{sl} is the pillar area fraction by definition.

13 Accordingly, the bending stress at their clamps is $\sigma_1 = \frac{\lambda_1}{\lambda_0}\frac{\sigma_0}{f_{sl}}$ and thus in general: $\sigma_n =$

14 $\frac{\lambda_n}{\lambda_0}\frac{\sigma_0}{f_{sl}{}^n}, \sigma_0 = \frac{2\mu N}{\pi r_0^2}\lambda_0$, $\lambda_n = \frac{2l_n}{r_n}$. The robustness of the structure is guaranteed at each

15 hierarchical level if $\sigma_n < \sigma_f$ where σ_f is the material failure strength. Thus, the failure

16 takes place for a nominal pressure $p_f = \frac{\sigma_f f_{sl}{}^n}{2\mu\lambda_n}$, from where the gain of having a frictionless

17 (μ at the denominator) and anticrack (σ_f at the numerator) material is evident. Eventually,

18 for having a critical load independent from the hierarchical level the rule is $\lambda_n \propto f_{sl}{}^n$ ($f_{sl}{}^n$

19 must be substituted by the production of the pillar area fractions if these are not identical).

20 (ii) When the load $N = pA$ is applied to the nominal area A, a buckling of the pillars could

21 take place at each hierarchical level for a buckling stress $\sigma_n = \frac{\pi^2 E}{4\lambda_n^2}$ where E is the material

22 Young's modulus. Accordingly, for avoiding instability at the hierarchical level n we have

23 $\sigma = \frac{p}{f_{sl}{}^n} < \sigma_n$ (σ is the effective applied normal stress on the pillar at that level). Thus

24 having a instability load $p_i = \sigma_n f_{sl}{}^n$ independent from the hierarchical level would

25 require $f_{sl}{}^n/\lambda_n^2 = const$. Here hard materials are preferred for avoiding instability, that

26 however compromises robustness only if crushing -se next point- takes places. In any case

27 instability for soft materials can be reduced by reducing the pillar slenderness.

28 (iii) Against crushing the pillars at the first hierarchical level collapse onto the zero-order

29 level macropillar; they can survive if in the collapsed configuration the stresses generated

30 are smaller than the material strength. Such stresses can be calculated from geometrical

31 considerations. In this case the minimum thickness δ_1 after compaction can be obtained by

32 a volume conservation, $i.e.$, $A\delta_1 = n\, l_1 A_1 / \eta$ where $A_1 = \pi r_1^2$ and η is the compaction

33 index (1 for total compaction). Geometrically the maximal strain is $\varepsilon_1 \sim k \frac{r_1}{\delta_1}$ with k constant

34 of the order of the unity. Assuming a (nonlinear) simple bilinear constitutive law of the

35 type $\sigma = E\varepsilon \;\; for \;\; \varepsilon < \varepsilon_l \;\; or \;\; \sigma = E\varepsilon_l + E_{nl}(\varepsilon - \varepsilon_l) \;\; for \;\; \varepsilon \geq \varepsilon_l$ and assuming

36 $\varepsilon_1 / \varepsilon_l = c \geq 1$ (maximal strain larger than ultimate linear strain) we obtain $\sigma_1 \sim \frac{2k\eta E_{eff}}{\lambda_1 f_{sl}}$

37 where $E_{eff} = E_{nl} + (E - E_{nl})/c$ is the effective Young's modulus and in general for

38 robustness (here rather than a pressure p is imposed the maximal displacement for full

39 compaction) at all the hierarchical levels $\sigma_n \sim \frac{2k\eta E_{eff}}{\lambda_n f_{sl}} < \sigma_f$. Note the advantage of having

40 a low Young's modulus E and even lower tangent Young's modulus of the nonlinear

41 regime E_{nl} in the presence of large relative deformation c for achieving a smaller effective

42 Young's modulus and thus a larger robustness that could be defined as $R \sim \frac{\sigma_f}{\sigma_n} = \frac{\sigma_f \lambda_n f_{sl}}{2k\eta E_{eff}}$.

43 Eventually, having a critical stress independent from the hierarchical level n would require

44 $\lambda_n = const.$ and the advantage of having soft linear (small E), and nonlinear (small E_{nl})

45 constitutive regimes with large failure strength (σ_f) is evident for robustness (R).

46 An optimization could be proposed requiring same resistance for mechanisms (i) and (ii)

47 ($i.e.$, same failure pressure) and minimal robustness for avoiding crushing (iii) failure ($i.e.$,

48 R=1) finding $\lambda_n^{(opt)} \sim \frac{\pi^2 E \mu}{2\sigma_f}$ and $f_{sl}^{(opt)} \sim \frac{2k\eta E_{eff}}{\sigma_f \lambda_n}$. For example, considering for Teflon

49 E=540MPa, $\mu = 0.08$ and σ_f =25MPa would result in $\lambda_n^{(opt)} \sim 8.5$, and similar to the

50 experimental observation.

51

52 **2. Mechanism for thermally fusing Teflon with substrate**

53 Teflon is extremely inert and anti-stick at normal conditions, and thus is hard to bond with

54 almost any other material using glue. Here, to create a strong adhesion between Teflon and

55 substrate, we laminated the Teflon material and substrate under conditions of elevated

56 temperatures (> 350 °C) and pressure (0.5 MPa), which resulted in a defluorination reaction

57 and formation of hydrocarbon-type carbon in the contacting interface. The interfacial

58 reaction significantly increases the surface energy of the contact interface and thus leds to

59 good interfacial bonding via physical adsorption.

60 **3. Thermal stability of soft silicone mold**

61 A prerequisite of pursuing the MPS strategy is a method to mass produce vast numbers of

62 true-3D microstructures as textures on a piece of Teflon. Before this work, however, no

63 method fulfills this requirement. Recently we created a method using a soft silicone mold's

64 configurable elasticity and shape memory to replicate 3D microstructures into

65 thermoplastics. As some of the Teflon materials, such as PFA and FEP, are thermoplastics,

66 in theory, they can be thermally shaped using this soft molding strategy. However, owing

67 to their high melting temperatures, Teflon should be processed at temperatures close to

68 300 °C. This temperature requirement makes it impossible to use our previous soft molding

69 recipe based on the silicone elastomer in the Teflon 3D imprinting process. It is because at

70 high temperatures such as 300 °C, the soft mold made of ordinary silicone materials will

71 be subject to thermal degradation and become brittle, leading to crack formation in the soft

72 mold, thereby the failure of the imprinting (Fig. S2A). The most critical molecular

73 reactions that account for the phenomenon are the scissions of Si-O and Si-C bonds through,

74 first, a depolarization chain reaction, leading to cyclic oligomer formation, and second, a

75 chain termination, leading to methane formation. Such reactions decrease the content of

76 flexible chains in PDMS, and lead to material cracking. To enhance the thermal stability

77 of the soft mold, we used 6 wt% Fe_2O_3 nanoparticles (30 nm in average diameter) as a

78 thermal stabilizer, and the mold was cured stepwise at 50 °C intervals from 150 to 300 °C,

79 with each step taking 30 min. This modification improves the thermal stability of the soft

80 mold significantly compared with conventional molds, as demonstrated in the long-term

81 baking and thermogravimetric analysis (Fig. S2). The mechanism is that the iron oxide will

82 prevent PDMS from oligomer formation by binding the oxide's surface hydroxyl groups

83 with the silanol groups formed in heated PDMS. Also, these iron oxide nanoparticles may

84 serve as soft crosslinks that maintain the flexibility of PDMS during baking at elevated
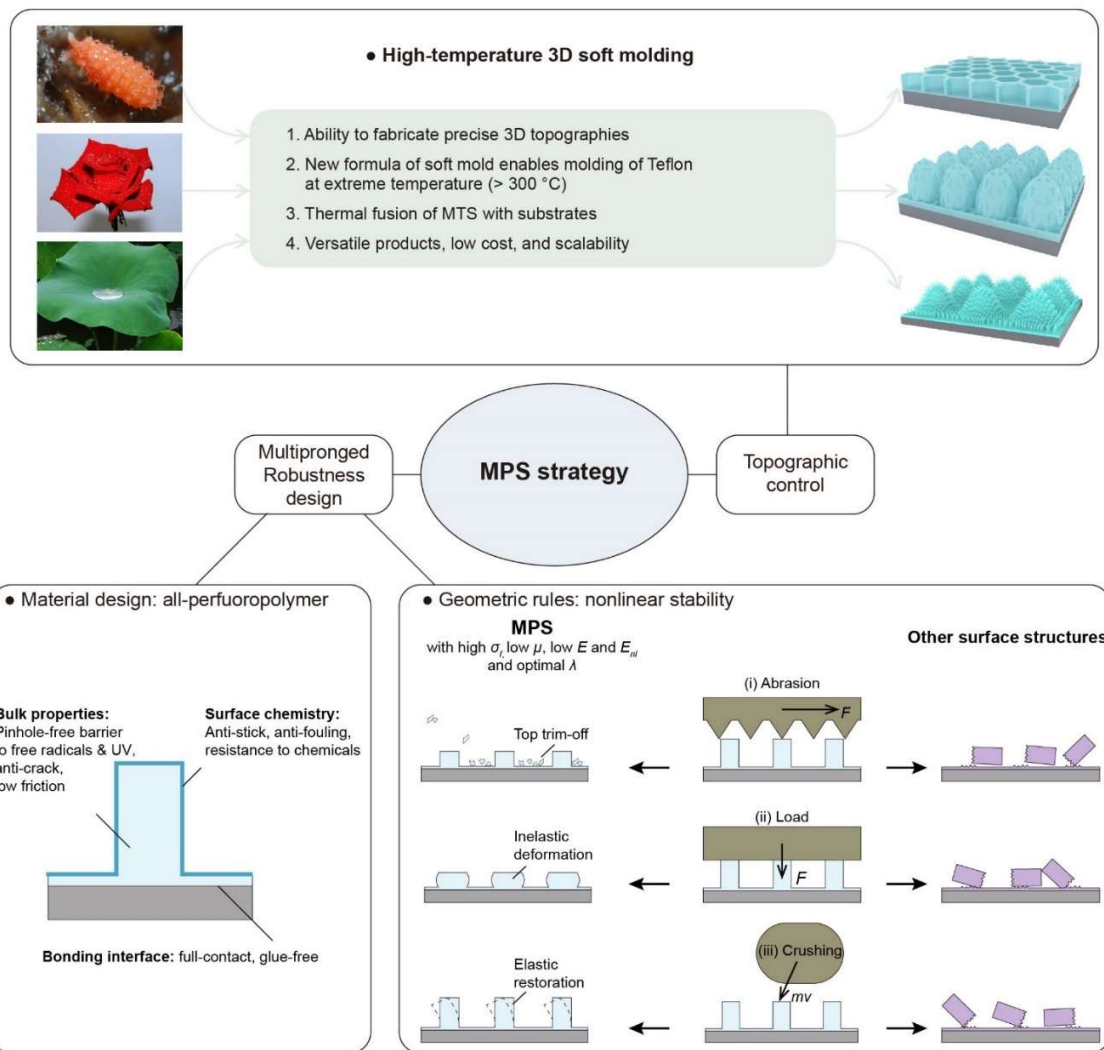
85 temperatures.

4. Characterized the topology-specific superwettability

87 We characterized the topology-specific superwettability of the surfaces, including the

88 springtail-inspired cavities with double reentrant, rose petal-inspired micro protuberances,

89 and lotus-inspired hierarchical pillars, as presented in Figure 3 in the manuscript. Although

90 the surfaces commonly manifest two-tier structures in micro and nano scale, their

91 wettability can be very different. The radar map in Figure S4 plots the water contact angle,

92 roll-off angle, droplet adhesion, pressure stability, and restitution coefficient for the three

93 MPS surfaces. First, the doubly reentrant cavities kept nonwetting and air retention even

94 in 9-m deep water (Fig. 3D), although its water contact angle is the smallest among the

95 three surfaces. Whereas, the other two surfaces were easily broken through by water under

96 pressure and lost their liquid repellency. Second, the micro protuberance arrays manifested

97 a large contact angle (> 150°) yet with a high droplet adhesion, which can be leveraged to

98 transfer microdroplets with minimized liquid fouling and consumption. On the contrary,

99 the other two surfaces cannot transfer droplet due to the little droplet adhesion or complete

100 water pinning. Third, the hierarchical pillars possessed the largest water contact angle and

101 smallest roll-off angle compared with the other two surfaces. Droplet impact on the surface

102 can bounce off at a restitution coefficient of ~0.7, comparable to that for superhydrophobic

103 lotus leaf, thus achieving self-clean of dirt.

5. Self-cleaning against particulate matters (PMs)

105 A common practice in demonstrating the self-cleaning function of a coating is to use water

106 to remove sand/soil from the coating surface. However, we doubt whether this strategy is

107 sufficient to demonstrate the real performance outdoors, because ambient PMs are in two

108 size ranges of 0.1-2 μm and ≥2 μm, respectively (Fig. S6A). In our speculation,

109 nanoparticles, known as "accumulation mode" PMs, deposit facilely into the features on

110 the surface with high adherent strength owing to their small sizes and the high surface-to-

111 volume ratios, and thus are hardly removable by impinging water droplets. As a result, the

112 free energy of the surface becomes higher. On this account, we performed comparative

4

113   self-cleaning experiments using iron oxide particles of micro- and nanosizes on

114   superhydrophobic coatings made of Teflon, PP, PE, and PDMS, respectively with the same

115   textures (Fig S6B and Supplementary Video 2). Microparticles (~2-μm) were easily taken

116   away from all the superhydrophobic coatings by impinging water droplets, even from the

117   superhydrophobic coating made of PDMS, a material well known for adhering dust.

118   However,when nanoparticles (~200 nm) were deposited on the surfaces, only the MPS

119   could be cleaned by impinging water droplets, and other surfaces could not be cleaned even

120   after further rinsing with high-pressure water jet. This result is consistent with the result

121   discussed above—the MPS was still superhydrophobic after being placed outdoors for 1

122   month, whereas others failed within a week (Fig. S7). Such superior performance may be

123   attributed to the nonstick property of Teflon, in which carbon atoms are surrounded by

124   closely packed F atoms, excluding the weak interactions that commonly take place on other

125   surfaces.

126

127

128

Fig. S1. MPS strategy. The MPS strategy includes three key components including (i) high-temperature 3D soft molding method, (ii) all-perfluoropolymer material design, and (iii) nonlinear geometric rules. First, we develop a high-temperature soft 3D imprinting process by creating a new soft mold formula that can work at temperatures higher than 300 °C. The method enables us to fuse perfluoropolymers with diverse substrates directly thermally and then fabricate precise 3D microstructures on the surface, with prolonged lifespan, improved fidelity, and product versatility and scalability. Second, the all-perfluoropolymer design primarily ensures robustness at different levels. At the coating-substrate interface, MPS possesses conformal and maximum bonding area by thermal fusion, thus tremendously improving the substrate adhesion. At the bulk level, MPS is a

139 pinhole-free and thick enough barrier to prevent all the free radicals, corrosive vapor and
140 gas from directly destroying the underlying substrate. At the surface level, MPS is anti-
141 stick, anti-fouling, and resistant to almost all chemicals, all of which are promising for
142 controlling air/liquid/solid matters for functional applications, such as self-clean, air
143 trapping, liquid transport, anti-fogging. Third, we developed theoretical models for
144 describing the robustness of MPS against friction-driven bending, elastic instability, and
145 nonlinear crushing (see Supplementary Text 1 for the details), the modeling suggests the
146 ideal robust MPS should have high failure strength σ_f, low friction μ, low Young's modulus
147 E and even lower tangent Young's modulus of the nonlinear regime $\boldsymbol{E_{nl}}$. Also in
148 counterintuitive contrast to the conventional assumption, the modeling demonstrates that
149 for a topologic surface, a moderate slenderness λ and nonlinear regium can be utilized for
150 improve its mechanical robustness.

151
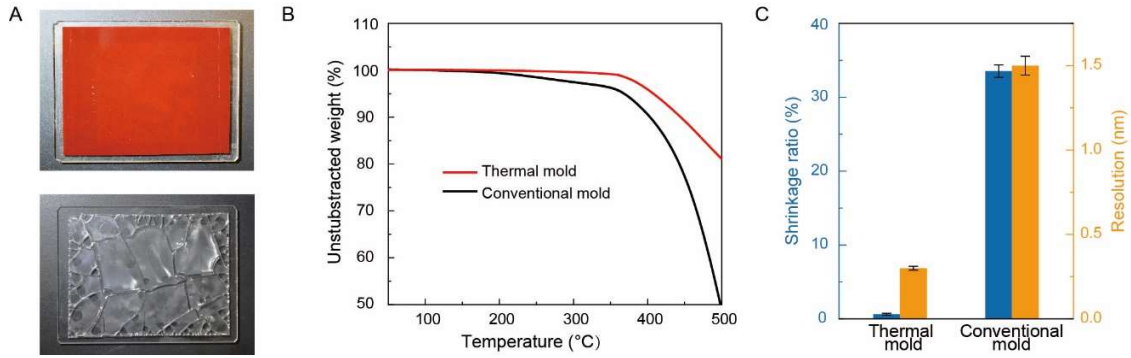
Fig. S2. Thermal-resistant soft mold with iron particles sufficiently stable for 3D imprinting Teflon materials. (A) Images showing the thermal molds with 6% Fe_2O_3 (upper image) and pure PDMS mold (lower image) after a baking process at 300 °C. The mold with 6% Fe_2O_3 kept intact after being baked for one week (upper image), while the pure conventional PDMS mold cracked after only 30 min baking (lower image). (B) TGA analysis of two soft molds. The unsubtracted weight of pure conventional PDMS mold decreased along with baking time, suggesting continuous degradation. In contrast, the thermal mold did not show noticeable subtraction during the baking process. (C) Comparison of the shrinkage ratio after heating and molding resolution between the thermal mold and conventional mold. The thermal mold experienced little shrinkage and enabled high molding resolution down to 300 nm.
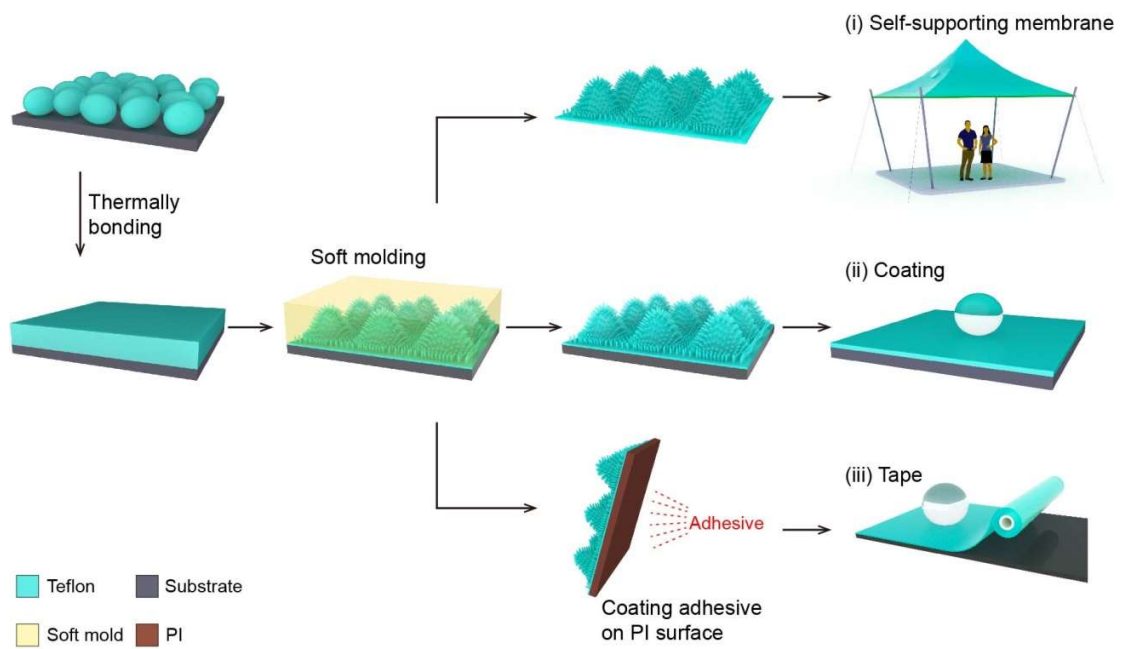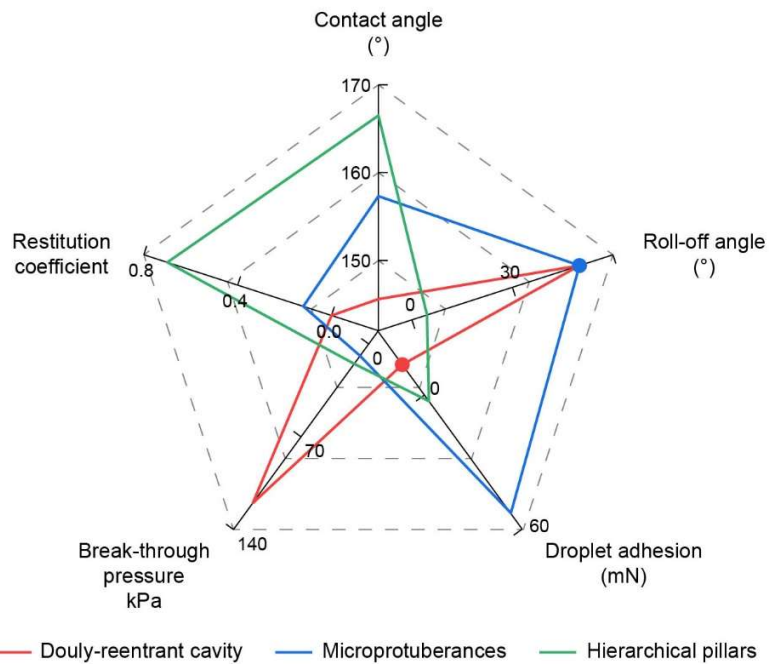
165

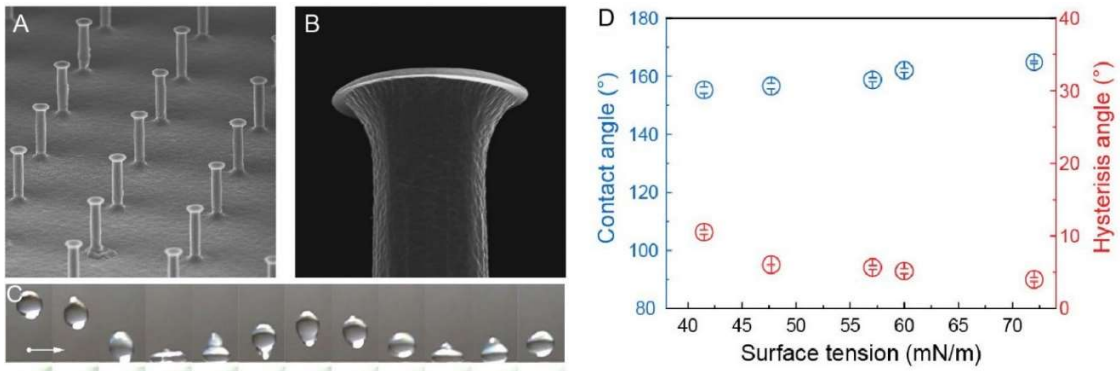166 **Fig. S3. Schematic illustration of the MPS fabrication.**

167

Fig. S4. A radar map showing the topology-specific superwettabilities on the three surfaces. The red dot denotes the failure to obtain adhesion force between the droplet and doubly reentrant cavities due to the complete pinning. The blue dot denotes the pinning of the droplet.

174

Fig. S5. Superamphiphobic MPS reentrant pillars with repellence to low-surface-tension liquids. (A) SEM image of the pillar array. (B) Zoom-in image of the thin reentrant on the top of each pillar. (C) Optical images showing a droplet of 15%wt ethanol in water bouncing on the surface. (D) Super-repellence to liquids with low surface tension. The liquids of different surface tension values were prepared by mixing water with ethanol at different ratios.
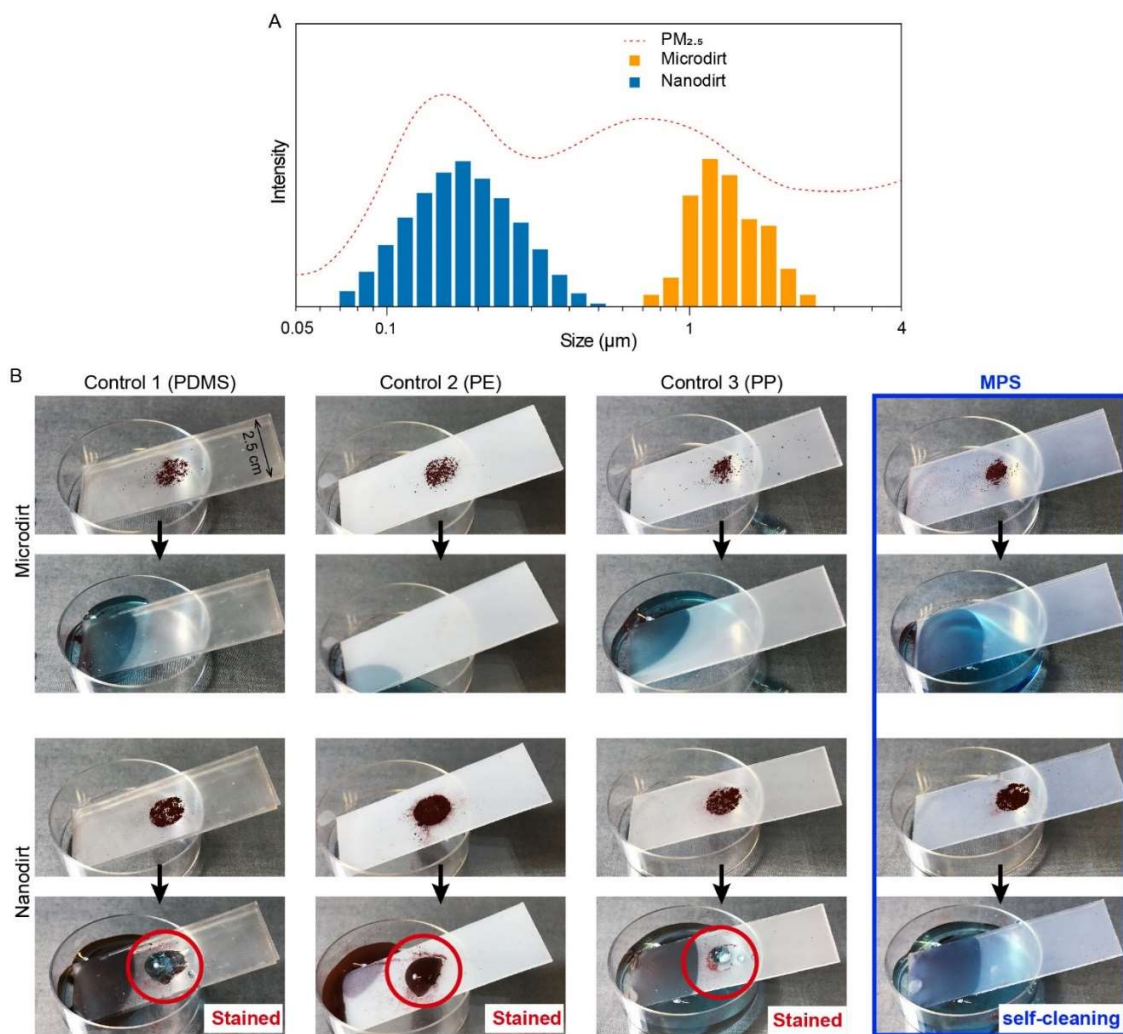
182
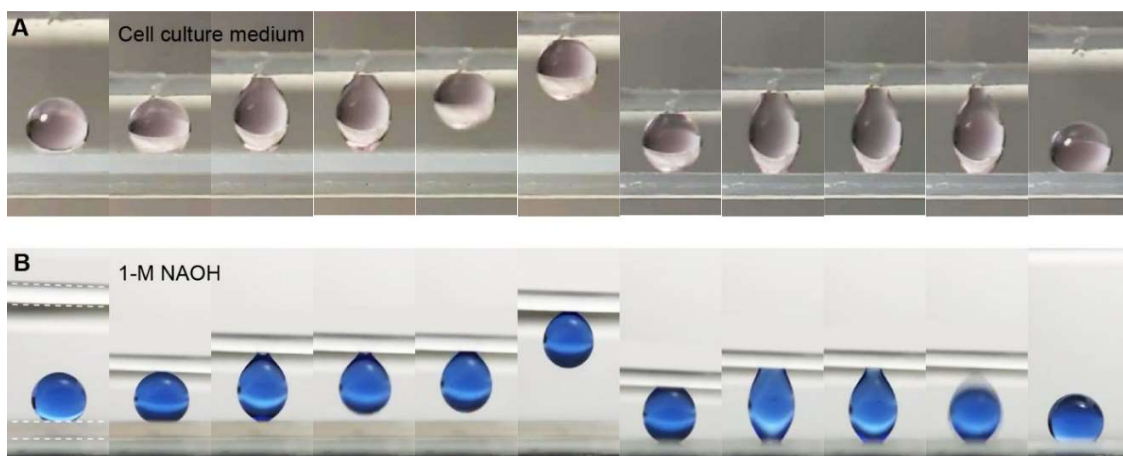
Fig. S6. Droplet transportation. The optical images show (A) a droplet of cell culture medium (Ham's F-12K (Kaighn's) Medium) and (B) a droplet of 1-M NaOH aqueous solution transported with the MPS surface mimicking rose petal.

187

Fig. S7. MPS with an enhanced self-cleaning performance against nanosized dirt. (A) Size distribution of the two groups of particle dirt, corresponding to the typical size distribution of PM2.5 in ambient air. (B) Representative images captured during the dirt removal tests. The ~2-μm dirt was easily removed from all the surfaces by rolling water droplets. In contrast, only MPS can self-clean ~200-nm dirt. All the surfaces in the test possess the same topology. See supplementary Video S5 for the details.
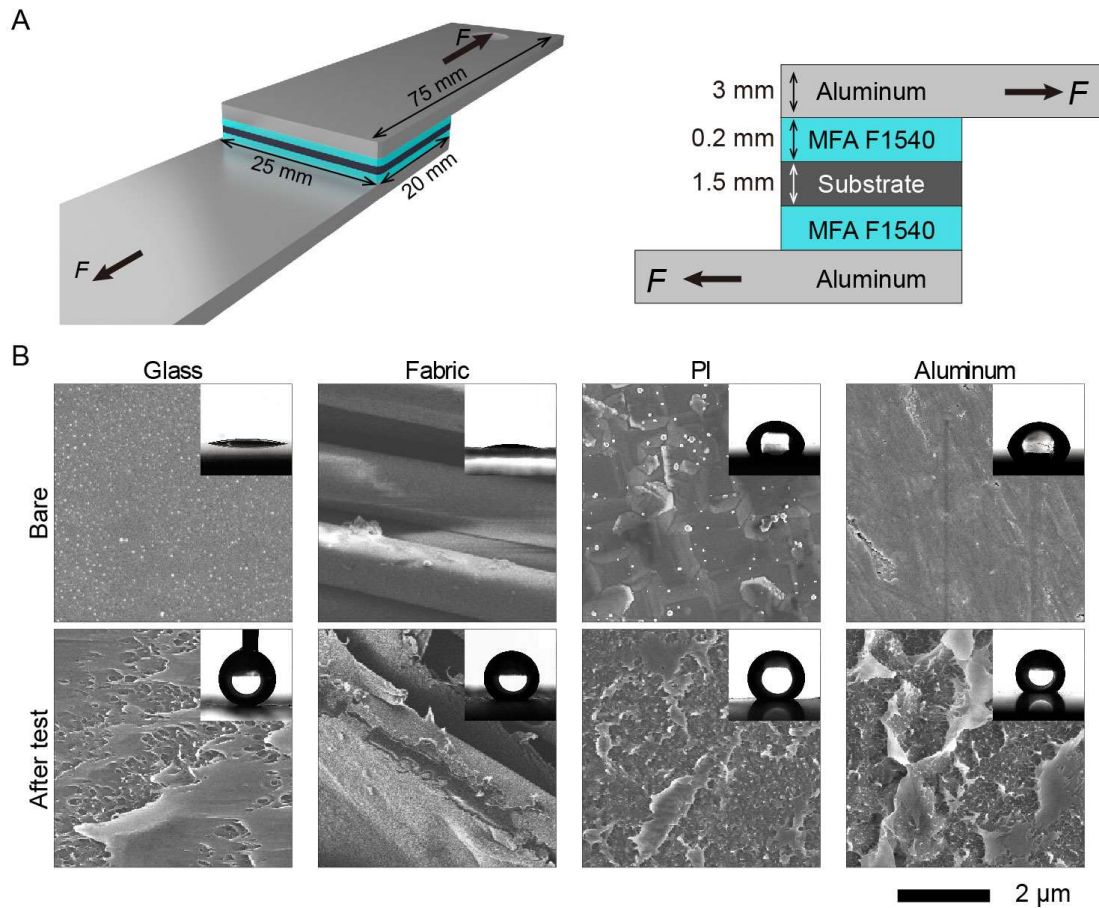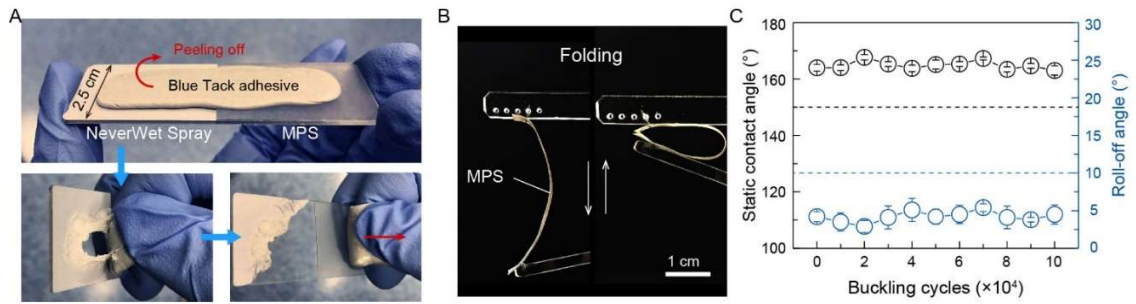
194

195
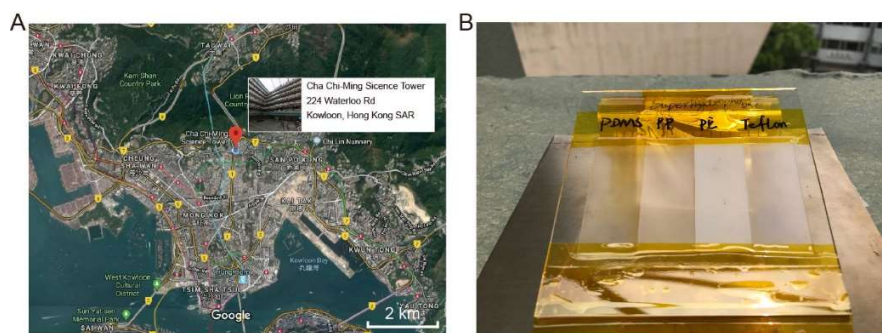
Fig. S8. Outdoor self-cleaning test of MPS for one month. The test location is in the urban area of Hong Kong city where the level of ambient fine particulate matter contamination is similar to other typical megacities. The average values of meteorological elements of the month for testing were recorded according to the information from Hong Kong Observatory. On average, the air temperature was 27.7 °C, the relative humidity was 78%, the total rainfall was 327.6 mm, and the average wind speed was 11.4 km/h. After one month, only the MPS surface remained superhydrophobic. (A) A map of the location of the tests. Reproduced from Google map, Copyright 2017 Google. (B) The superhydrophobic coatings were placed on the roof of the Science Tower of Hong Kong Baptist University for one month. PDMS, polyethylene (PE), polypropylene (PP) superhydrophobic surfaces with the same topology were used for comparison.

207

A

3 mm ↕ Aluminum ⟶ F
0.2 mm ↕ MFA F1540
1.5 mm ↕ Substrate
MFA F1540
F ⟵ Aluminum

B

| | Glass | Fabric | PI | Aluminum |

208

Fig. S9. Substrate adhesion test by shear stress model. (A) Geometric model and the bonding assembly for the test. (B) SEM images of the substrate surface before and after the tests. The upper-row images show the bare substrates with their inherent wettability. The lower-row images show the substrates detached from the Teflon, with Teflon residuals left on all the surfaces, making all the substrates surfaces superhydrophobic. Insets show the contact angle measurements using 3-μl water droplets.

215

Fig. S10. Robustness of the MPS against peeling and folding. (A) The peeling test using a pressure-sensitive rubbery adhesive, which was applied onto the surfaces under ~500 KPa for 5 min, and then peeled off slowly. The NeverWet spray coating was easily peeled off together with the adhesive within several cycles, while both the bonding interface and surface texture of MPS were intact after peeling the adhesive. (B and C) Folding test. (B) The folding model. (C) Relationship between the water repellence of the surface and the folding cycles. The blue and red dash lines denote the boundaries of superhydrophobicity ($\theta^* > 150°$ and $\theta_{roll\text{-}off} < 10°$). The error bars are standard deviations obtained from five independent measurements.

227
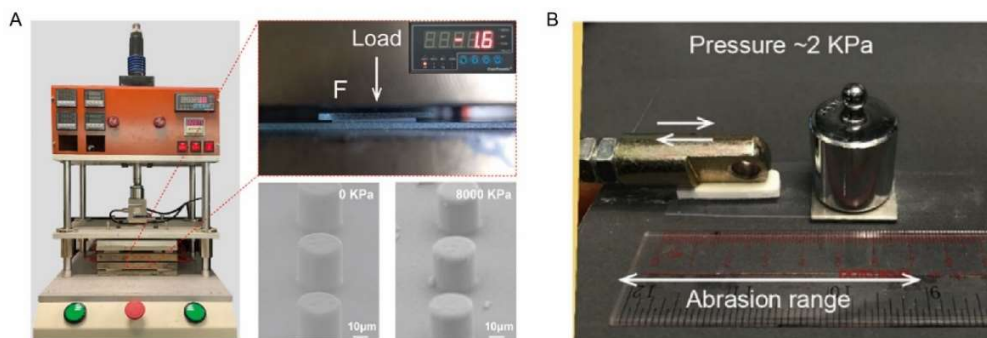
Fig. S11. Models for mechanical robustness tests. For the experimental validation of the theoretical prediction, a MPS pillar array with an initial slenderness λ ~8 and liquid/solid contact fraction f_{sl} ~10% was employed. (A) Pressing test, the sample with an area of 1×1 cm^2 was placed in a compressing machine, with the load being driven by compressed gas and precisely controlled by a gas valve. For the pressing test, a static load was applied on the sample for 10 min. To investigate the structural robustness of the Teflon pillars, pressures from 0 to 16 MPa were applied on pristine samples. (B) Abrasion test, the pillar side on a MPS sample (2×2 cm^2) was made contact with 1200-Cw sandpaper, and a weight of 100 g, i.e., 2.5 KPa pressure, was applied to the stack. The MPS sample was pushed for 10 cm along the ruler and back to the original point.
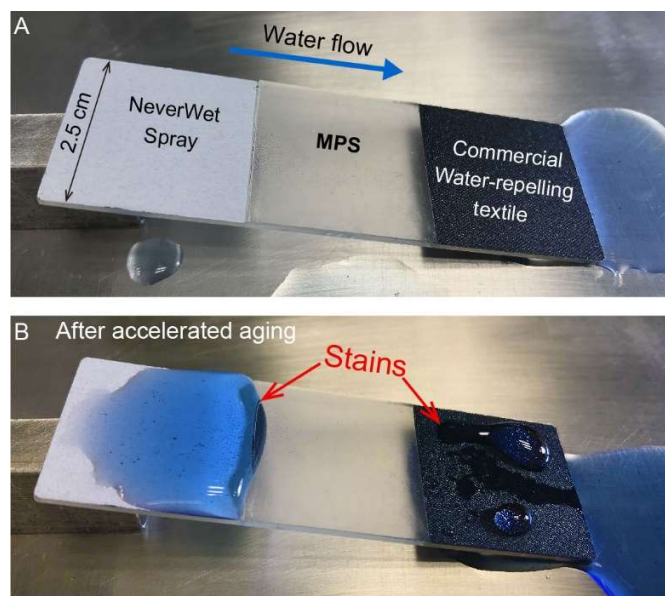
238
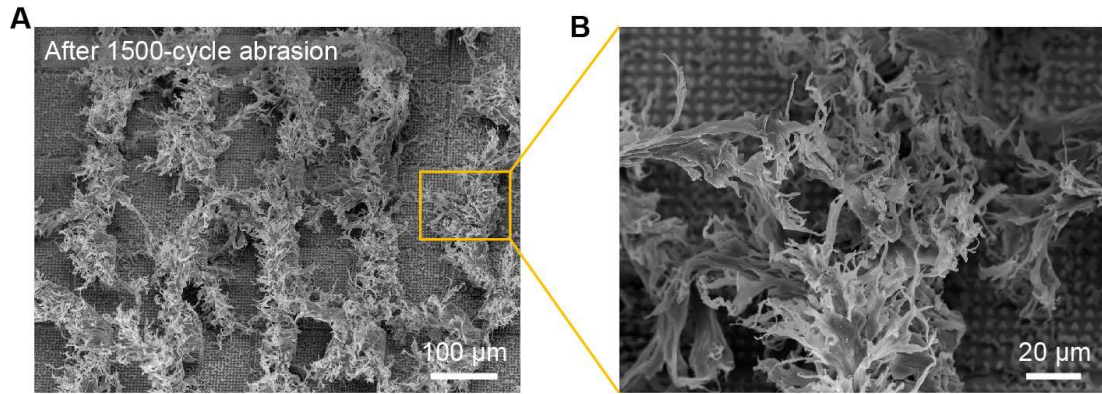
Fig. S12. SEM image of dense nano-sized hairs regenerated on the tops of the micropillars during abrasion (A) and a zoom-in view (B).

243

Fig. S13. Aging robustness tests. Three samples, including a high-quality commercial
spray coating (NeverWet, gray), MPS (transparent), and a water-repellence textile (black)
were mounted on a glass slide. Water dyed blue was dropped onto the upper end of the
slide and flowed over the three samples to examine their water repellence. (A) All the fresh
samples showed strong repellence to water. (B) After the aging test, the MPS remained
superhydrophobic whereas the other two became hydrophilic. Note the water staining on
the two regions in (B).

251

252
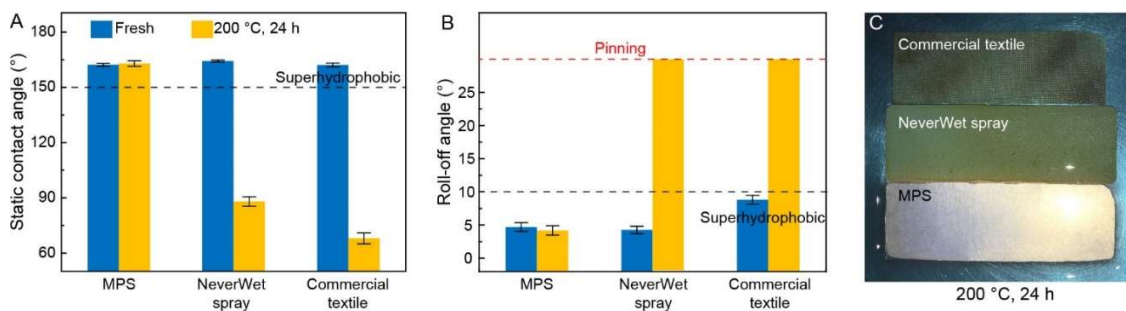
Fig. S14. The thermal stability tests. The commercial water-repelling textile and high-quality water-repelling spray tested in Fig.S12 were also tested for comparison. These samples were heated at 200 °C for 24 h. Static contact angles (A) and roll-off angles (B) of the fresh and thermally treated materials were measured before and after the tests, respectively. (C) Image of three samples immersed in blue-colored water after the thermal treatment. The results indicate that MPS remained superhydrophobic, whereas the control samples already changed to hydrophilic. All the error bars are standard deviations obtained from five independent measurements.

Table S1. Summary of the unique topographies and functionalities of both natural and artificial superhydrophobic surface.

Species	Material	Topology	Scale range of hierarchical structure	Functionality	Reference
Lotus	Biomaterials	Hierarchical pillars	~5 nm - 10 μm	Enhanced superhydrophobicity	*Planta* 202, 1–8 (1997)
Springtail	Biomaterials	Double reentrants	~200 nm - 5 μm	Enhanced suspension force to low-surface-tension liquids	*PLoS One* 6, e25105 (2011)
Rose petal	Biomaterials	Micropapillae with nanofolds	~200 nm - 20 μm	Droplet capture	*Langmuir* 24, 4114–4119 (2008)
Cicada wing	Biomaterials	Ordered nanopillar arrays	~50 nm	Transparency, bactericidal, enhanced self-cleaning	*Small* 8, 2489–2494 (2012)
Butterfly wing	Biomaterials	Hierarchical nanoplates	~100 nm - 3 μm	Structural color, directional adhesion	*Soft Matter*, 3, 178–182 (2007)
Water striders	Biomaterials	Microsetae with nanogrove	~50 nm - 50 μm	Enhanced floatage	*Nature*, 432(7013): 36-36 (2004)
Diving flies	Biomaterials	Micro hairs	~1-30 μm	Stable air entrapment	*PNAS*, 114, 13483-13488 (2017)
Mosquito compound eyes	Biomaterials	Microspheres with nanonipples	~100 nm - 26 μm	Dry-style antifogging	*Adv. Mater.* 19, 2213–2217 (2007)
Salvinia leaf	Biomaterials	"Egg-beater" hairs	~20-1000 μm	Enhanced floatage and air entrapment	*PNAS*, 117(5): 2282-2287 (2020)
Artificial	Silica	Micropillars with double reentrant	~200 nm - 20 μm	Repellence to completely wetting liquids	*Science* 346, 1096–1100 (2014)
Artificial	Copper	Hierarchical pillars	~10 nm - 400 μm	Droplet reshape and contact time reduction	*Nat. Phys.* 10, 515–519 (2014)
Artificial	Silica	Macroedge with nanoroughness	~100 nm - 2 mm	Split droplet and contact time reduction	*Nature* 503, 385–8 (2013).
Artificial	FEP	Microtrench with nanoroughness	~500 nm - 1 mm	Stable air entrapment	*Phys. Rev. Lett.* 113, 1–5 (2014)
Artificial	Silica	Micro inverted pyrimid with nanocandle soots	~50-100 μm	Armor for protecting nanoassembly	*Nature*, 582(7810): 55-59 (2020)
Artificial	Silica	Honeycomb cavities with double reentrants	~500 nm-100 μm	Stable air entrapment and mitigating cavitation erosion	*Nat. Commun.* 9, 1–11 (2018)

Table S2. References for summary of multi-level indexs of existing superhydriphobic surfaces

Synthetic coatings		Micro-machined surfaces	
Method	**References**	**Method**	**References**
Nano assembly	*Science*, 299, 1377 (2003)	Photolithography/plasma etching	*Science*, 318, 1618 (2007)
Nano assembly	*Science*, 347, 1132 (2015)	Lithography/etching/embossing	*Nature*, 582, 55 (2020)
Nano assembly	*Science*, 335, 67 (2012)	Photolithography/plasma etching	*Science*, 346, 1096 (2014)
Nano assembly	*Nat. Mater.*, 17, 1040 (2018)	Wire cutting machine	*Nat. Phys.* 10, 515 (2014)
Nano assembly	*Nat. Mater.*, 17, 355 (2018)	Micromachine	*Nature*, 503, 385 (2013)
Nano assembly	*Nat. Mater.*, 12, 315 (2013)	3D Printing	*PNAS*, 117, 6323 (2020)
Nano assembly	*Adv. Mater.*, 29, 2 (2017)	Photolithography/plasma etching	*Nature*, 527, 82 (2015)
Nano assembly	*Adv. Mater.*, 29, 1702517 (2017)	Photolithography/plasma etching	*Sci. Adv.*, 4, eaat4978 (2018)
Nano assembly	*Adv. Mater.*, 24, 2409 (2012)	Photolithography/plasma etching	*Phys. Rev. Lett.*, 106, 1 (2011)
Nano assembly	*Nat. Commun.*, 6, 8649 (2015)	Photolithography/plasma etching	*Nat. Phys.*, 12, 606 (2016)
Nano assembly	*Adv. Mater.*, 23, 2962 (2011)	2D Transfer molding	*Adv. Mat.*, 32, 2002710, (2020)
Nano assembly	*Nat Commun.*, 12, 982 (2021).	Photolithography/plasma etching	*Nat. Commun.*, 9, 1 (2018)
Nano assembly	*Langmuir.*, 27, 9597 (2011)	Photolithography/plasma etching	*Adv. Funct. Mater.*, 21, 4617 (2011)
Nano assembly	*J. Am. Chem. Soc.*, 135, 578 (2013)	Embossing	*ACS Nano*, 11, 9259 (2017)
Nano assembly	*Chem. Eng. J.*, 381: 122539 (2020)	Femtosecond laser	*J. Mater. Chem.*, A, 6, 9049, (2018)
Nano assembly	*Chem. Eng. J.*, 399, 125746 (2020)	Etching	*ACS Nano*, 14, 10198, (2020)
Nano assembly	*Chem. Eng. J.*, 398, 125403 (2020)	Etching	*J. Mater. Chem.*, A, 6, 9049, (2018)
Nano assembly	*ACS Appl. Mater. Inter.*, 12, 48216 (2020)	Nanosphere lithography	*ACS Nano*, 10(10), 9379, (2016)

Nano assembly	*ACS Appl. Nano Mater.*, 3, 2047-2057 (2020)	Etching	*J. Mater. Chem. A*, 3, 21797, (2015)
Nano assembly	*Adv. Funct. Mater.*, 24, 986 (2014)	Lithography/DRIE	*Sci. Adv.*, 6(13), eaax6192, (2020)
Nano assembly	*Adv. Mater.*, 32, 1908008 (2020)	2D Nanoimprint	*Adv. Funct. Mater.*, 30, 2004227, (2020)
Nano assembly	*Chem. Eng. J.*, 358, 1610-1619 (2019)	Interference lithography	*Small*, 10, 2487, (2014)

1

2

Table S3. Rubrics for the comparison of strategies to produce biomimetic coatings/surfaces.

Index	Topological functionalities	Mechanical robustness	Chemical resistance (e.g., chemicals, aging)	Substrate adhesion	Radiation resistance	Eco-friendliness
5	Able to mass-fabricate arbitrary 3D micro/nano structures with precisely controlled shapes on arbitrary surfaces	Can tolerate simultaneously long-distance, high-load abrasion and vertical compression at high pressures	Resistant to strong solvents, strong reactive species (strong acids/alkalis/corrosives/oxidants), moisture, and heat in all over very long period of time	Withstand hundreds of cycles of rubbery adhesive peeling. No coating mass loss during the peeling test. Adhesion strength comparable to strong commercial glue. Withstand bending of the substrate.	Withstand long-term exposure to highly reactive radiations, at least including UV, plasma, and corona at elevated temperatures.	No toxic molecules or persistent pollutant particles released over long period of aging under harsh environment; fully recyclable
4	Able to mass-fabricate true-3D micro/nano structures with controlled shapes	Can tolerate both long-distance abrasion and vertical compression	Resistant to strong solvents, strong reactive species (strong acids/alkalis/corrosives/oxidants), moisture, and heat over considerable period of time	Withstand hundreds of cycles of tape (e.g., 3M VBH) peeling with heavy preset load. No significant coating mass loss during the peeling test. Adhesion strength close to commercial glue.	Withstand long-term exposure to UV at high temperatures.	Little number of toxic molecules or persistent pollutant particles released over long period of aging under mild environment; production process might involve toxic chemicals
3	Able to mass-fabricate semi-3D structures as a coating on surfaces	Can tolerate either long-distance abrasion or vertical compression	Resistant to either strong solvents or reactive species over a limited period. Resistant to moisture and heat over	Withstand tens of cycles of tape (e.g., 3M VBH) peeling with heavy preset load.	Able to survive certain period of UV radiation and can self-heal for multiple	Release a small number of toxic molecules or persistent pollutant particles over time; production process

			considerable period of time.		cycles after the exposure.	involves toxic chemicals
2	Able to fabricate microstructures on a specific substrate or generate random hierarchical roughness on a surface	Can tolerate short-distance abrasion or vertical compression at moderate pressures	Resistant to moisture and heat over a limited period	Withstand limited cycles of tape peeling without load.	Able to survive certain period of UV radiation.	Release a considerable number of toxic molecules or persistent pollutant particles over time; production process may cause pollution
1	Only able to generate random roughness on a specific substrate	Can only tolerate mild abrasion or mild pressure	Poor resistance to solvent/corrosion/oxidation	Cannot withstand tap-peeling.	Only able to survive a very short period of UV radiation.	Easily release a large number of toxic molecules or persistent pollutant particles, production process may cause severe pollution.

1

Supplementary Video. 1. Low-fouling transportation of liquid droplets using MPS. Droplets of serum, cell culture medium (Ham's F-12K (Kaighn's) Medium), and 1-M NaOH solution, respectively, on a low-adhesion surface (lotus texture), were first captured by a high-adhesion surface (rose petal texture) and then transferred to another high-adhesion surface (rose petal texture).

Supplementary Video. 2. Self-cleaning tests of MPS. Some other superhydrophobic surfaces made of polypropylene, polyethylene, and polydimethylsiloxane were used for comparison. This movie is divided into three parts. 1. Water droplets slipped off the superhydrophobic surfaces, effectively removing the iron oxide microparticles from all samples. 2. Water droplets slipped off the surfaces but were only able to take away the iron oxide nanoparticles from the MPS surface. The other surfaces lost their **superhydrophobicity caused by non-cleanable nanoparticle contamination.**

Supplementary Video. 3. Mechanical robustness test of MPS. This movie includes four parts. 1. Buckling test. The buckling test was performed with a homemade device. 2. Press test by a female adult (~52.5 kg weight) standing on two samples. 3. Abrasion test of the MPS surface with sandpaper (Starcke, P600). 4. Examination of water repellence. Blue dyed water was dropped onto the sample surfaces (at a tilt angle of 5°) to verify the water repellence.

Supplementary Video. 4. Car compression test. This video demonstrates the real usage of MPS. The superhydrophobic surfaces made of Teflon (MPS, right), PP (middle), and PS (left) were placed at the front door of Hong Kong Baptist University on Kam Shing Road for 2 hours. After the compression test, only MPS surface maintained full water repellence, and PP surface showed a certain degree of repellence. While the sample made of Teflon illustrated the optimum performance of the MPS strategy, the sample made of PP illustrated the satisfactory performance of a surface made of another material fulfilling the guideline rules of MPS (material toughness and slenderness). In contrast, the sample made of PS demonstrated the weak mechanical robustness of a surface containing the same topology,

when the material does not fulfill the guideline of the MPS strategy. PS is a material with low toughness, despite it possessing sufficient hardness.

Supplementary Video. 5. Finger wiping test. In this demonstration, an MPS and a Teflon superhydrophobic surface with random structures (which does not follow the MPS slenderness rule) were compared regarding their robustness. Both were superhydrophobic initially, as evidenced by the rolling-off water droplets at a tilt angle of ~7°. After several rounds of gentle wiping using a finger, the random Teflon surface already pinned the water droplet, while in sharp contrast, our MPS surface was still superhydrophobic.

Supplementary Video. 6. Chemical robustness test. In this test, a high-quality commercial water-repelling spray coating (NevertWet, left), and a commercial water-repellent textile (right) were employed to compare with the MPS (middle). The water repellence was examined by blue-colored water flowing over the surface, and the samples before and after the exposure under harsh conditions (70 °C, 254-nm UV) for 12 h were compared.